OpenDVP: An experimental and computational framework for community-empowered deep visual proteomics

Jose Nimo[1,2], Sonja Fritzsche[1,3], Daniela S. Valdes[1], Minh Trinh[1], Tancredi Pentimalli[1,2,4], Simon Schallenberg[5], Frederick Klauschen[6,7,8], Florian Herse[1,2,9], Stefan Florian[5], Nikolaus Rajewsky[1,2,4] and Fabian Coscia[1,*]

[1]Max-Delbrück-Center for Molecular Medicine in the Helmholtz Association (MDC), Berlin, Germany

[2]Charité – Universitätsmedizin Berlin, corporate member of Freie Universität Berlin and Humboldt-Universität zu Berlin, Berlin, Germany

[3]Humboldt-Universität zu Berlin, Institute of Biology, Berlin, Germany

[4]Laboratory for Systems Biology of Regulatory Elements, Berlin Institute for Medical Systems Biology (BIMSB), Max-Delbrück-Centrum for Molecular Medicine in the Helmholtz Association (MDC), Berlin, Germany

[5]Institute of Pathology, Charité – Universitätsmedizin Berlin, corporate member of Freie Universität Berlin and Humboldt-Universität zu Berlin, Berlin, Germany

[6]Institute of Pathology, Ludwig Maximilians University Hospital Munich, Munich, Germany

[7]German Cancer Consortium (DKTK), Partner Site Munich, and German Cancer Research Center (DKFZ), Heidelberg, Germany

[8]BIFOLD - Berlin Institute for the Foundations of Learning and Data, Berlin, Germany.

[9]Experimental and Clinical Research Center, a cooperation between the Max-Delbrück-Center for Molecular Medicine in the Helmholtz Association and the Charité - Universitätsmedizin Berlin, Germany

*To whom correspondence should be addressed: fabian.coscia@mdc-berlin.de

Abstract

Deep visual proteomics (DVP) is an emerging approach for cell type-specific and spatially resolved proteomics. However, its broad adoption has been constrained by the lack of an open-source end-to-end workflow in a community-driven ecosystem. Here, we introduce openDVP, an experimental and computational framework for simplifying and democratizing DVP. OpenDVP integrates open-source software for image analysis, including MCMICRO, QuPath, and Napari, and uses the scverse data formats AnnData and SpatialData for multi-omics integration. It offers two workflows: a fast-track pipeline requiring no image analysis expertise and an artificial intelligence (AI)-powered pipeline with recent algorithms for image pre-processing, segmentation, and spatial analysis. We demonstrate openDVP's versatility in three archival tissue studies, profiling human placenta, early-stage lung cancer, and locally relapsed breast cancer. In each study, our framework provided insights into health and disease states by integrating spatial single-cell phenotypes with exploratory proteomic data. Finally, we introduce deep proteomic profiling of cellular neighborhoods as a scalable approach to accelerate spatial discovery proteomics across biological systems.

Introduction

Recent advances in spatial omics have revolutionized our understanding of tissue biology and disease processes [1]. In particular, spatial proteomics is experiencing remarkable progress in sensitivity, throughput, and spatial resolution [2]. The ability to map proteins with high spatial resolution has provided novel insights into cellular organization, tissue heterogeneity, and disease mechanisms with unprecedented detail. The significance of these advancements lies in the premise that proteomic profiles provide a direct perspective on the functional and phenotype-centric cellular states that govern health and disease. Historically, spatial proteomics has depended on targeted, antibody-based methodologies [3], which offer excellent spatial resolution, yet require prior knowledge for antibody panel design. Antibody-based methods, which profile up to ~60 proteins [4], capture a comparatively small fraction of the proteome, which is estimated to encompass more than 10,000 different proteins per single cell type [5]. A highly synergistic approach involves integrating targeted methods with ultrasensitive liquid chromatography-mass spectrometry (LC-MS)-based proteomics. This multiscale approach has paved the way for exploratory, comprehensive analyses of cell-type and spatially resolved tissue proteomes [6,7]. Recently, we co-developed deep visual proteomics (DVP)[8], which combines tissue imaging (immunofluorescence [IF] or immunohistochemistry [IHC]), machine learning-based image analysis, automated laser microdissection (LMD), and ultrasensitive MS for the exploratory proteomic profiling of cell types or regions of interest (ROI). DVP enables the systematic mapping of thousands of proteins, elucidating their networks and signaling pathways within complex tissue architectures, and providing unprecedented insights into health and disease states. For example, DVP was recently used to discover a curative treatment strategy for a fatal human skin disease [9] and to map single-cell proteotoxicity in human liver [10].

However, the full potential of DVP has been constrained by the lack of open-source workflows for scalable image analysis, laser microdissection support, and multimodal data integration. Moreover, there is a growing demand for simplified experimental strategies, supporting researchers with limited experience in image analysis and spatial proteomics. To address this, we developed open-source deep visual proteomics (openDVP). We built openDVP as a highly modular framework, allowing scientists to customize their own approach based on specific research needs and available

resources while integrating the latest advancements in bioimage analysis and computational proteomics. OpenDVP is equipped with state-of-the-art image processing and spatial analysis tools optimized for high-performance computing and incorporates the latest advances in ultrasensitive, high-throughput MS-based proteomics to acquire hundreds of spatially resolved proteomes. We show our framework's versatility in three archival tissue studies and demonstrate how cellular neighborhood-guided proteome profiling, compared to more challenging single-cell isolation, offers a powerful and balanced approach for spatial discovery proteomics at scale.

Results

Overview of the openDVP framework

We developed openDVP, an open-source and modular framework for user-empowered deep visual proteomics (**Fig. 1a**) (https://github.com/CosciaLab/openDVP). Our end-to-end framework encompasses optimized functions for all the key steps of the DVP workflow, supporting image preprocessing and analysis, automated laser microdissection, interactive image data visualization, and multimodal data integration. OpenDVP supports the most common imaging and proteomics data formats by current and extending functionalities from existing open-source software, such as MCMICRO[11], SOPA[12], QuPath [13], Napari [14], and SpatialData [15]. Importantly, the modules' inputs and outputs are standard file formats for seamless integration of community-published or in-house tools. We introduce two complementary workflows: a simplified fast-track pipeline, termed flashDVP, which does not require image analysis expertise, and an extended AI-powered pipeline capable of in-depth spatial tissue analyses. FlashDVP serves as an intuitive entry point for users seeking to rapidly convert raw images (i.e., H&E, IHC, or IF) into exploratory spatial proteomics results. The extended AI-powered DVP workflow enables more experienced users to customize and optimize the pipeline using advanced single-cell spatial analysis tools for more complex phenotype-to-proteotype associations.

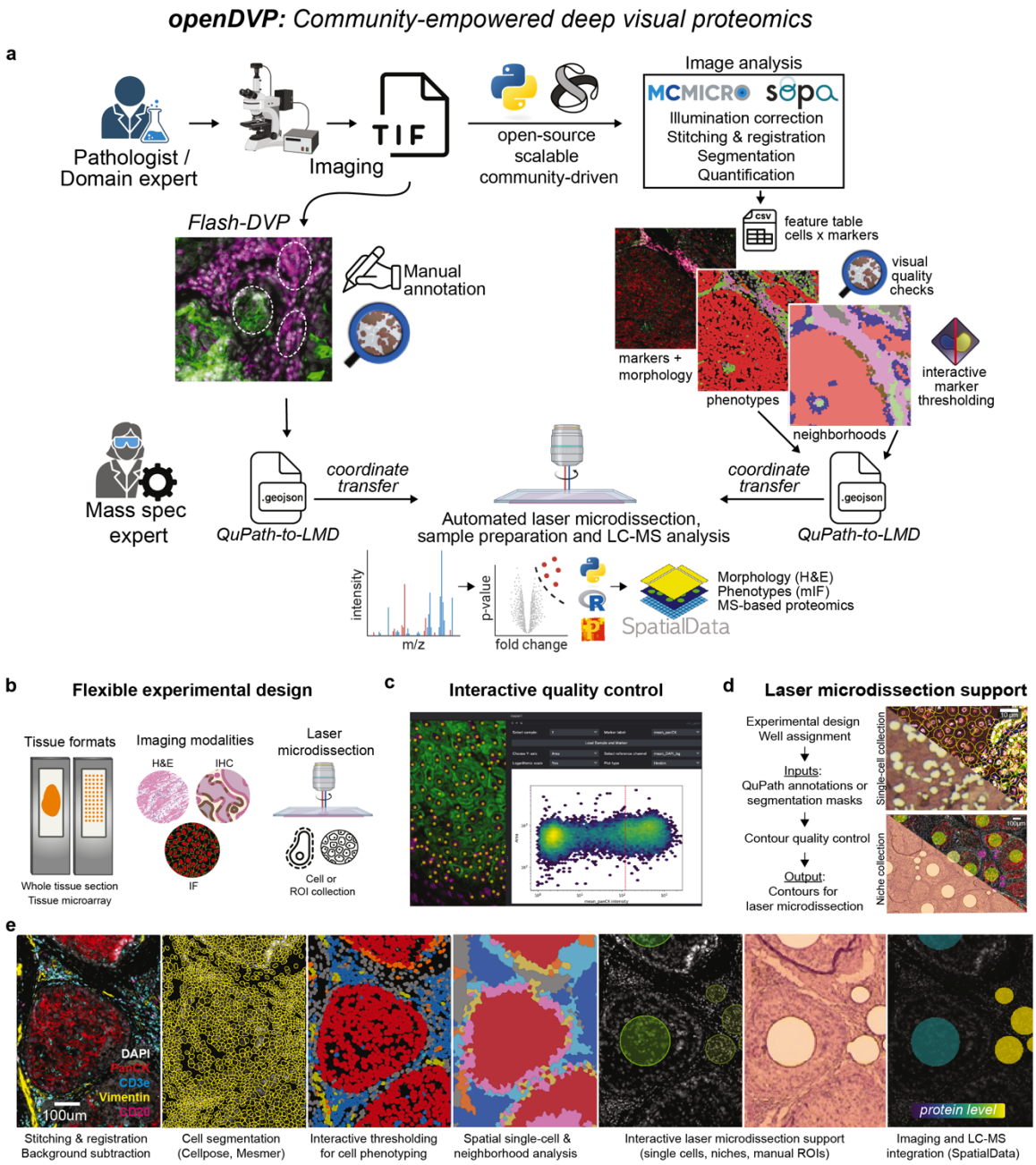

Fig. 1: Overview of the openDVP framework

(a) Main workflow of openDVP begins with tissue imaging to produce TIFF files. Flash-DVP comprises manual image annotation, coordinate transfer with the QuPath-to-LMD webapp, and laser microdissection. OpenDVP provides a framework to process images into feature tables and analyze matrices to phenotype cells, using open-source tools. These data layers provide the basis for contour export and laser microdissection via QuPath-to-LMD. **(b)** OpenDVP supports tissue microarrays or whole-slide images, common imaging modalities, and different LMD collection strategies. **(c)** The Napari-cell-gater plugin enables phenotyping through visual feedback thresholding, plotting cell features in FACS-like density plots. **(d)** QuPath-to-LMD webapp allows users to design, transfer, and validate annotations from QuPath and openDVP to an LMD-ready file format. **(e)** Exemplary openDVP workflow showing the results of multiplexed immunofluorescence (mIF) imaging, cell segmentation, cell phenotyping, cellular neighborhood analysis, contour annotations, and multimodal data integration using SpatialData.

Providing a versatile solution to support diverse spatial proteomics experiments

We built openDVP for compatibility with a wide range of imaging applications that support whole-slide images (WSI) and tissue microarrays (TMA) based on conventional widefield or confocal microscopy (H&E, IHC, IF, and mIF) (**Fig. 1b**). While WSI can provide a comprehensive view of large tissue areas, which are particularly important for heterogenous tissues, TMA applications support cohort-size spatial proteome analyses. Importantly, the imaging pipelines use BioFormats compatible file formats (e.g., OME-TIFF) and does not rely on any proprietary software or specific microscopy hardware for broad accessibility.

Efficient and extensible image processing

Following image acquisition, the first step in DVP workflow is the processing of images, including illumination correction and stitching image tiles. OpenDVP builds on top of the established open-source image processing pipelines MCMICRO and SOPA (**Fig. 1a**). MCMICRO was built using NextFlow [16], following nf-core guidelines, to ensure high standards of modularity, consistency, and interoperability. SOPA is built on python-based Snakemake [17], enabling python-fluent users to add new modules or modify existing steps. We developed custom modules to expand segmentation masks by a defined number of pixels, quantify marker intensity quantiles per cell, and pyramidize images for smooth quality control. These open-source pipelines offer key advantages: (1) Broad compatibility, supporting most imaging formats and modalities. (2) Modular architecture, integrating latest algorithms and machine learning models, such as Cellpose 2.0 and DeepCell's Mesmer. (3) Scalability, enabling efficient distribution of processes, for example, segmenting about a million cells from centimeter-scaled whole slide images in less than 3 hours. (4) Active maintenance and development by a growing community of bioimage analysts.

Interactive quality control and marker thresholding for single-cell phenotyping

Visual quality control is critical in image processing pipelines to assess illumination correction, stitching and registration results, and segmentation accuracy. OpenDVP also provides demo datasets and Jupiter notebook-based tutorials to help users integrate and inspect results using two complementary interfaces, Napari and QuPath. We chose them for their ability to visualize larger-than-memory images and community activity in developing new features. To facilitate image-based cell phenotyping based on marker expression, we developed an interactive Napari plugin

(**Fig. 1c**) (github.com/CosciaLab/napari-cell-gater). Our plugin enables users to visualize multichannel images, overlay segmentation masks, plot mutually exclusive markers (FACS analysis-like), and provide real-time feedback of cells being labelled positive or negative based on selected thresholds. Although more laborious, this approach gives users full autonomy in their filter strategy for the complex task of single-cell phenotyping. For transparency, our plugin generates summary tables with cutoff values for each marker-sample pair. Finally, our image-processing pipeline creates a filtered single-cell matrix used for supervised or unsupervised analysis to identify cell types, states, and cellular neighborhoods. These guide laser microdissection and exploratory LC-MS-based proteome analysis.

A versatile interface between image analysis and laser microdissection

Laser microdissection is an essential step in the DVP workflow for isolating either single cells or ROIs in a precise and automated manner. Segmentation-based cell/nucleus isolation provides the highest biological granularity, which is particularly relevant for single-cell applications or rare phenotypes. The isolation of larger ROIs (e.g., multi-cellular niches) represents a robust alternative to single-cell LMD cutting. To support both scenarios for high user flexibility, we developed *QuPath-to-LMD*, an interactive open-source web app for experimental design support, contour export, and validation of LMD-ready masks, currently supporting the Leica LMD7 and MMI CellCut systems (**Fig. 1d**) (github.com/CosciaLab/Qupath_to_LMD).

Importantly, *QuPath-to-LMD* provides an accessible interface between histopathology and omics-based profiling, as histological slide annotations can be directly transferred into LMD-ready contours for downstream (prote)omic analysis.

Integrating imaging and MS-based proteomics data through the scverse ecosystem

DVP generates two types of proteomic data: imaging and LC-MS data. For data integration, visualization, and multi-modal analysis, openDVP's python code uses scverse standards and the AnnData and SpatialData formats, ensuring compatibility with popular analysis packages such as scimap [18], scanpy [19], and spatialproteomics [20]. To our knowledge, this framework represents the first instance of integrating mass spectrometry-based proteomic data into the scverse ecosystem, streamlining data analysis for large-scale spatial tissue proteomics. For example, through SpatialData adoption, users can overlay their images with cellular phenotype information (e.g., cell

types and cellular neighborhoods) and matching quantitative proteome information. We developed a data analysis package to facilitate storing, integrating, visualizing, and analyzing spatial proteomics data (**Suppl. Fig. 1**). A vignette of the openDVP workflow is shown in **Fig. 1e.**

OpenDVP quantifies cell-type resolved proteomes of human placental tissue

Understanding biological foundations of human health and disease requires comprehensive characterization of individual cells, the fundamental units of life. Recent single-cell and spatial omics advancements have catalyzed large-scale initiatives, such as the Human Cell Atlas [21] and the LifeTime Initiative [22], which aim to systematically profile all human cell types across tissues to unravel relationships between cells, tissue organization, and function. However, certain cell types (e.g., cardiomyocytes, adipocytes, and neurons) pose analytical challenges due to their resistance to dissociation into single-cell suspensions. Their interconnectivity and/or fragility make them inaccessible for sorting-based single-cell profiling, and they are often morphologically too complex for accurate cell segmentation. One example is the syncytiotrophoblast (STB) of the human placenta, a syncytial layer derived from fused cytotrophoblasts (CTB) that lacks distinct cell boundaries (**Fig 2a**), making cell segmentation and single-cell-based laser microdissection challenging. Despite STB's critical roles in nutrient exchange, hormone secretion, and immune modulation at the maternal-fetal interface [23], its syncytial nature has prohibited its comprehensive molecular profiling, particularly at the global proteomic level. With this in mind, we applied flashDVP as a simplified and image segmentation-free version of DVP. We performed four-color immunofluorescence (IF) staining of 5µm thick first trimester human placental FFPE sections mounted on PPS frame slides and performed centimeter-scale whole-slide imaging.

The placental barrier, appearing in tree-like villi structures, controls the nutrient and gas exchange between maternal and fetal blood. It consists of E-cadherin+ bipotential CTBs that fuse to form a multinucleated E-cadherin−, HLAG− STB layer that is in direct contact to maternal blood. HLAG+ trophoblasts constitute the invasive CTB derived lineage that anchor the placenta to the maternal uterine tissue (**Fig 2a**). CD163+ extraembryonic macrophages (Hofbauer cells, HBC) in the stroma play roles in tissue remodeling, immune surveillance, and support the formation and maintenance of fetal blood vessels in the villi [24]. We annotated 150 cells per replicate for each cell

type (STB, CTB, and HBC, **Fig 2c-d**) to reach an equal tissue amount per sample. LMD contours were created using the *QuPath-to-LMD* web app, transferred to a Leica LMD7 microscope for laser microdissection and processed using our ultralow-input tissue proteomics protocol [25]. Samples were measured in label-free diaPASEF mode and analyzed with DIA-NN [26] in library-free mode. We identified 3,994 unique proteins across groups (**Suppl. Fig. 2a**), including canonical markers for each cell type (**Fig. 2d, Suppl. Fig. 2c**). Principal component analysis separated cell phenotypes regardless of tissue origin (**Fig. 2e**). Differential abundance analysis revealed cell type-specific markers that showed good concordance with public transcriptomics data [27,28] (**Fig. 2f-g**). Pathway analysis of protein clusters confirmed STB-specific functions in steroid hormone metabolism, vesicular transport, and energy demands (**Fig. 2h**). The regulation of SUMO proteins, linked to placental development and hypertension in pregnancy in bulk studies [29,30], was specific to STBs despite their lower abundance, underscoring the value of cell-type resolved proteomic analyses. CTB and HBC showed an enrichment in RhoJ GTPase and VEGF signaling pathways, while HBCs displayed immune regulation pathways, supporting their immunotolerant role. We found HBC-specific enrichment for proteins involved in mRNA splicing, aligning with the role of alternative splicing as an essential feature of placental dysfunction [31]. Given the physical proximity between STBs and CTBs (**Fig. 2a, c**), cell communication analysis between these connected trophoblasts cells revealed high paracrine activity of both cell types, with autocrine communication strongest in the CTB monolayer (**Fig. 2i**). Strong signaling via cadherins (CDH), junctional adhesion molecules (JAM), fibronectins (FN1), and desmosomes was inferred, supporting the importance of cell adhesion integrity in fusion-competent CTBs. We identified robust communication involving collagens, laminins, and extracellular matrix proteins critical for implantation and placentation [32]. Our data also revealed that endothelial cell-selective adhesion molecule (ESAM) as a unique and previously unreported autocrine signaling molecule of STBs. ESAM is an important component of tight junctions and a negative regulator of platelet activation; the latter is known to underpin pregnancy health and coexist with complications [33]. These findings establish flashDVP as a powerful 'fast-track' approach for cell type and spatially resolved tissue proteomics.

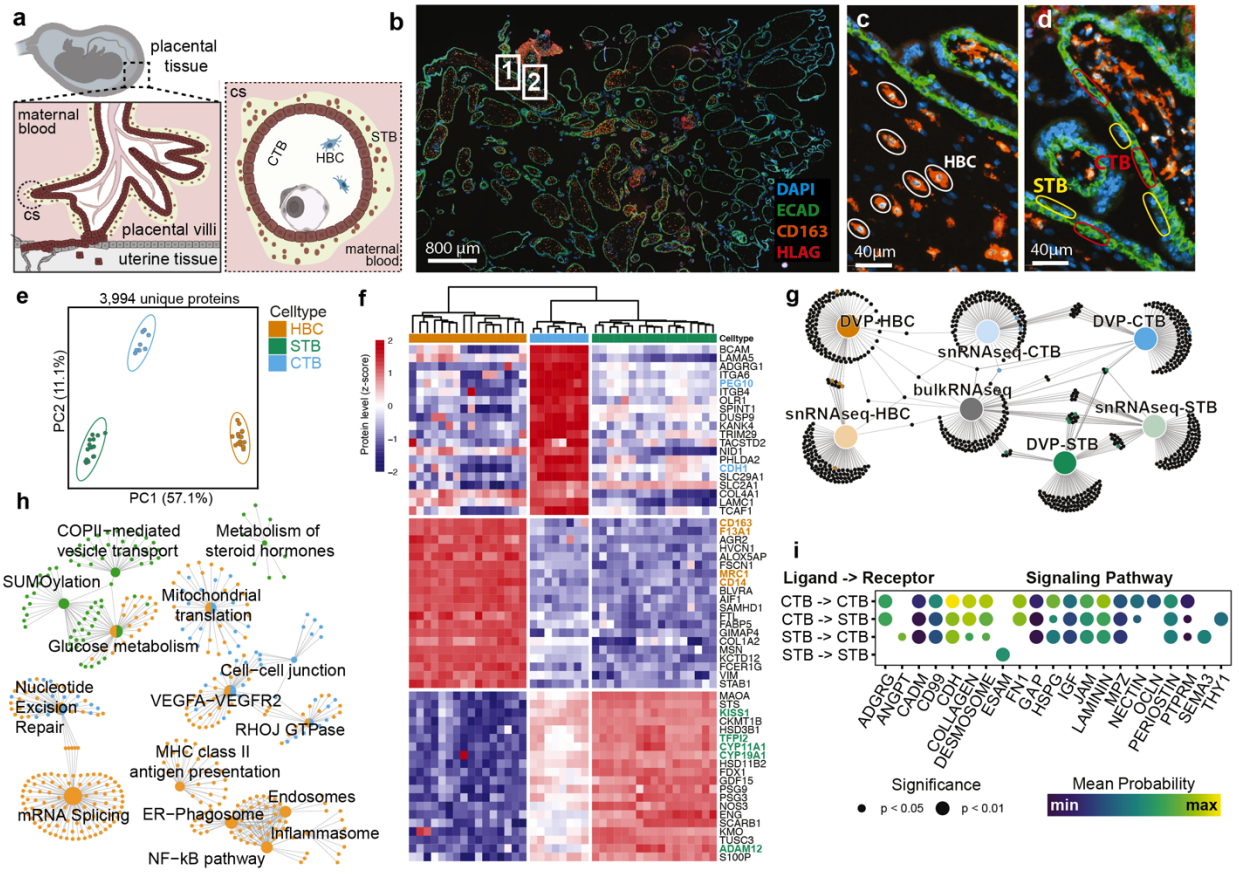

Fig. 2: High-resolution cell-type resolved proteomics of human placental tissue
(a) Left: Schematic of placental villi samples and fetal structures at the maternal-fetal interface. Right: Cross-section showing cytotrophoblast (CTB) monolayer replenishing syncytiotrophoblast (STB) layer, with Hofbauer cells (HBC) in the stroma. cs, cross-section. **(b)** Representative immunofluorescence image of placental tissue stained for E-cadherin, CD163, HLA-G, and DNA (DAPI), used for cell type annotation, laser microdissection, and proteomic profiling. Box inserts correspond to panels c (1) and d (2). **(c,d)** Representative regions of interest manually selected in QuPath for isolation of immune (c) and trophoblast (d) compartments. CTB monolayer is defined by E-cadherin+ and HLAG-, whereas the multinucleated STB layer is E-cadherin- and HLAG- in the outer layer of the villi. CD163 expression marks macrophages (HBC). **(e)** Principal component analysis of cell type resolved proteomes from three placental tissues. Colors indicate cell types. Confidence ellipses (95% CI) computed from PC scores covariance. **(f)** Cell type-specific protein marker heatmap as inferred by ANOVA (FDR < 0.05) showing relative abundance profiles per replicate. Canonical markers for each phenotype highlighted in orange (HBC), green (STB), and light blue (CTB). Z-scored relative protein abundances are shown. **(g)** Comparison of flashDVP-generated phenotype-specific proteins and published genes marking CTB, STB, and HBC phenotypes. Shared and unique markers highlight the importance of proteomic data in complementing other omics. **(h)** Enriched functional pathways of phenotype-separating clusters from (g). Enrichment based on ranked proteins using the Reactome database. Circle shows overrepresented proteins per pathway, color indicates cell phenotype. **(i)** Significant cell-cell communication in trophoblast compartment inferred using CellChat[34]. Dot colors show mean communication probability of ligand-receptor pairs in labelled pathway, size represents p-value from one-sided permutation test.

OpenDVP coupled to spatial transcriptomics uncovers niche-specific drug targets in an aggressive lung tumor

We next tested whether flashDVP could facilitate cell-type resolved tissue proteomics by integrating additional spatial omics layers. We analyzed a serial FFPE tissue section from an early-stage lung adenocarcinoma that we previously characterized by spatial transcriptomics (ST, Nanostring CosMx) [35] (**Fig. 3a**). Using 960 cancer-related genes, we profiled over 340,000 cells, identifying 18 cell types and their spatial distribution. These rich data revealed diverse immune and tumor cell niches of therapeutic value, including a small tumor niche enriched for pro-metastatic mesenchymal tumor cells with high NDRG1 and LGALS1 expression, located near myofibroblasts and SPP1+ tumor-associated macrophages (TAMs) (**Fig. 3b**). Pseudotime analysis identified this 'epithelial to mesenchymal (EMT)-niche' as the potential start site of tumor invasion. Based on these observations, we investigated the proteome of EMT-niche tumor cells to understand their functional state and to identify potential drug targets. IF staining of a serial tissue section against epithelial and mesenchymal markers, overlaid with CosMx phenotypes, confirmed the mesenchymal nature of EMT niche tumor cells (panCK+, VIM+, E-cadherin-) (**Fig. 3c-d**). We next annotated multiple ROIs to proteomically profile tumor and stromal niches (**Suppl. Fig. 3a**). ROIs contained 50-100 cells (40,000 – 50,000 μm^2, 5 µm thick). We quantified 4,138 and 4,976 proteins in stromal and tumor compartments respectively, totaling 5,956 proteins (**Fig. 3e, Suppl. Fig. 3b**). Group replicates clustered together and showed high proteome correlations (Pearson's r > 0.9, **Suppl. Fig. 3c**). PCA analysis showed EMT-niche tumor cells and stroma-infiltrating tumor cells were closer to stromal samples in component 1, reflecting their mesenchymal phenotype (**Fig. 3f**). Integration with CosMx data confirmed that tumor cell-intrinsic signatures dominated the EMT-niche tumor proteomes (**Fig. 3g-h**). Proteomics further validated the CosMx and IF data showing panCK+, VIM+, and E-cadherin- tumor cells in the EMT-niche and upregulated NDRG1 and LGALS1 protein levels. Many genes identified by ST were also significantly upregulated at the protein level in EMT niche tumor cells, emphasizing the value of spatial niche information in 3D for aligning and integrating tissue sections for multi-omics analyses (**Fig. 3a**). However, MS-based proteomics captured higher dynamic ranges of analyte abundances, resulting in different gene/protein rankings and drug target prioritizations (**Fig. 3g-h, Suppl. Fig. 3d**). We identified 133 additional FDA-approved drug targets upregulated in the EMT niche (**Suppl. Fig. 3e**),

including 46 cancer-related targets like PDGFRβ, an actionable gene for imatinib, a receptor tyrosine kinase inhibitor approved for various malignancies including gastrointestinal stromal tumors and myeloproliferative neoplasms [36]. SLC2A1/GLUT1 was the most up-regulated protein in EMT niche tumor cells. Consistently, pathway analysis revealed high glycolysis expression in EMT niche tumor cells, along with hypoxia, angiogenesis, and EMT pathways (**Suppl. Fig. 3f**). As targeting glucose metabolism is currently under clinical investigation for cancer therapy [37,38], we assessed the tumor-specific expression of GLUT1 and its association with patient outcomes. We validated high tumoral GLUT1 expression in a large-scale transcriptome study of 483 lung adenocarcinomas and 347 control samples [39,40] (**Fig. 3i)** as well as on IHC data obtained from the human protein atlas [41] (**Fig. 3j)**. High GLUT1 expression was a strong prognostic factor associated with poor patient outcome, as revealed by the significantly different overall survival (p = 0.0003, n=239 per group) (**Fig. 3k**). These data support the notion that targeting glucose metabolism, possibly via GLUT1, could offer a potential therapeutic strategy for targeting highly invasive and metabolically rewired lung cancer cells. Together, these results underline the benefit of cellular niche-guided spatial multiomics as a promising approach for identifying and validating niche-specific, personalized drug targets.

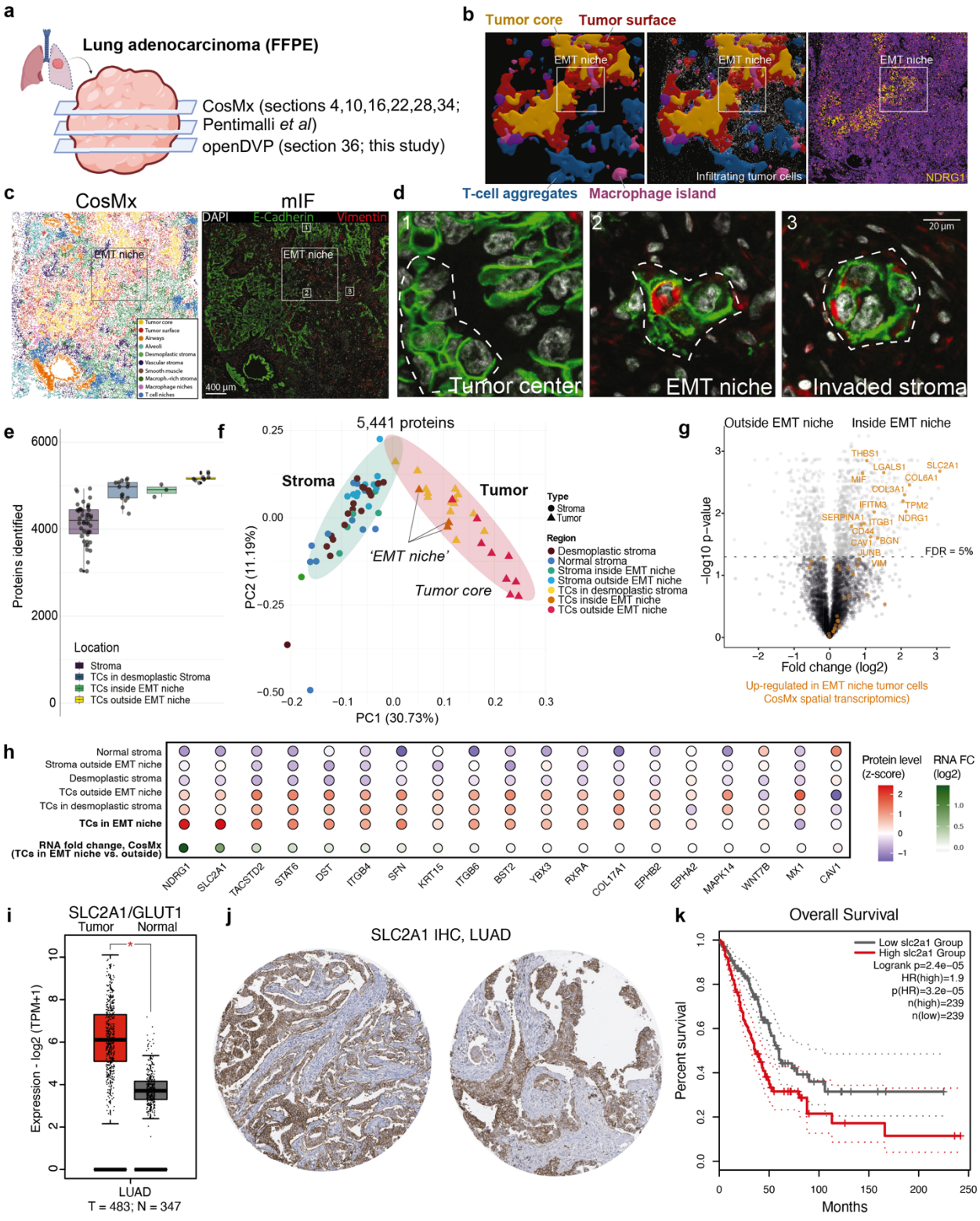

Fig. 3: Cell-type resolved deep proteomic profiling of transcriptionally defined cellular niches

(a) Overview of 5 µm FFPE lung adenocarcinoma sections showing regions for CosMx spatial transcriptomics and DVP analysis. **(b)** 3D reconstruction of transcriptomically defined niches, showing tumor-infiltrating cells. NDRG1 RNA level was upregulated in tumor cells from the surface and EMT niche, as previously published by us [35]. **(c)** Left: 2D multicellular niche map from CosMx data (Section 34[35]). Right: immunofluorescence of epithelial (E-cadherin,

green) and mesenchymal (vimentin, red) markers in section 36. Insets 1–3 correspond to panel (d). Nuclei with DAPI (white). Scale bar: 400 µm. **(d)** Magnified views: [1] tumor center (E-Cadherin+/Vimentin-), [2] EMT niche (E-Cadherin+/Vimentin+, arrow), and [3] invading tumor cells (E-Cadherin+/Vimentin+, arrow). Scale bar: 20 µm. **(e)** Proteomics identified a mean of 4,138 proteins in stroma and 4,976 in tumor regions (50–100 cells/sample). **(f)** Principal component analysis of 5,441 proteins shows a separation of tumor and stroma samples along PC1. EMT niche tumor samples cluster near invasive and stromal samples. **(g)** Volcano plot showing differential protein abundance in tumor cells inside vs. outside the EMT niche. CosMx-upregulated genes [35] in orange. **(h)** Relative protein levels of top upregulated genes in EMT niche tumor cells. **(i)** Mean RNA expression of SLC2A1/GLUT1, the most EMT-niche upregulated tumor protein in the proteomics data, in lung cancer cohort (n = 483 tumor, 347 healthy; TCGA LUAD) shows higher expression in cancer tissues [39]. **(j)** GLUT1 IHC staining of lung adenocarcinoma tissues confirmed tumor-specific expression. Images (left: ID 426; right: ID 1303) from human protein atlas [41]. **(k)** Kaplan–Meier analysis showed lower overall survival in patients with high SLC2A1/GLUT1 RNA expression, grouped by median.

OpenDVP uncovers broad tumor microenvironment remodeling in primary and locally relapsed triple-negative breast cancer

Tumor ecosystems comprise spatially defined clusters of immune, stromal, and epithelial cells with distinct pro- and anti-tumorigenic functions. Such cell communities, or cellular neighborhoods (CNs), are associated with therapeutic responses and patient outcomes across cancer types [42–44]. Triple-negative breast cancer (TNBC), the most aggressive breast cancer subtype [45], exemplifies how tumor microenvironment (TME) organization and CNs associate with distinct clinical outcomes [46]. For example, recent studies have revealed critical roles of CNs comprising tumor-associated macrophages (TAM) and cancer-associated fibroblasts (CAFs) [47–49]. A detailed understanding of CNs within the TME hence offers new treatment avenues by identifying druggable proteins that mediate cellular interactions and communication. We reasoned that CN-guided proteome profiling would offer a robust approach to accelerate spatial discovery proteomics while retaining the DVP core concept to connect visual phenotypes with quantitative proteomes. To address this, we first derived an optimized protocol for centimeter-scale whole-slide multiplex immunofluorescence (mIF) imaging on PPS membrane slides and included a panel of nine markers for this proof-of-concept study (**Fig. 4a-b**). We stained and imaged two paired tissue sections obtained from the primary surgical resection and matching local relapse sample of the same patient. The primary sample showed a large (38 mm) ductal carcinoma in situ (DCIS) that invaded the surrounding stroma at several sites (**Fig. 4c, subplot 2**), thus transitioning to invasive carcinoma. The relapse manifested two years later after systemic adjuvant chemotherapy and featured a large (45 mm in diameter) focus of invasive carcinoma without any residual DCIS. Both image datasets (each 150GB+) were processed using MCMICRO and SOPA for cell segmentation, phenotyping, and neighborhood analysis. H&E staining of the same slide allowed

us to integrate additional tissue morphology information (**Suppl. Fig. 4a-b**). We segmented 610,182 and 1'005,051 cells from the primary and relapse sample, respectively, that clustered into five major communities corresponding to cancer cells, T-cells, B-cells, macrophages, and stromal cells (**Fig. 4c-e, Suppl. Fig. 4c-d**). In both primary tumor and relapse, panCK+ tumor cells were most abundant, followed by T lymphocytes and stromal cells. Cell type frequencies differed significantly between the two tissue samples (**Fig. 4f)**. CD3+ T-cells were the second most abundant population in the primary sample, which localized with CD20+ B-cells in the stroma around DCIS-filled ducts (**Fig. 4c, subplot 1**). The relapse sample showed reduced CD20+ B-cells and CD8+ T-cells, while CD68+ macrophages and VIM+ stromal cells increased 16-fold and 4-fold, respectively (**Fig. 4f**), supporting their role in cancer progression and immune evasion [50,51]. These data revealed microenvironmental remodeling from a small, therapy-naïve carcinoma to a resistant secondary tumor. To evaluate the consequences of these cell type-specific changes on spatial tissue architecture, we performed cell neighborhood analysis. Using scimap's spatialLDA algorithm, we identified seven recurring CNs with distinct cell proportions (CN0-6, **Fig. 4g**). CN0, CN1, and CN6 showed strongest abundance differences between the two samples **(Fig. 4g-i)**. Proximity analysis revealed CD68+ macrophages were more distant to tumor cells in the primary sample compared to the relapse, while B and CD8+ T cells were in higher proximity (**Fig. 4j**). This demonstrated spatial reorganization from an initial lymphocyte-rich infiltrate surrounding the emerging tumor in the primary sample towards a macrophage rich infiltrate located inside the large relapsed tumor. These phenotypic differences prompted us to investigate the underlying biological processes associated with treatment resistance and tumor recurrence.

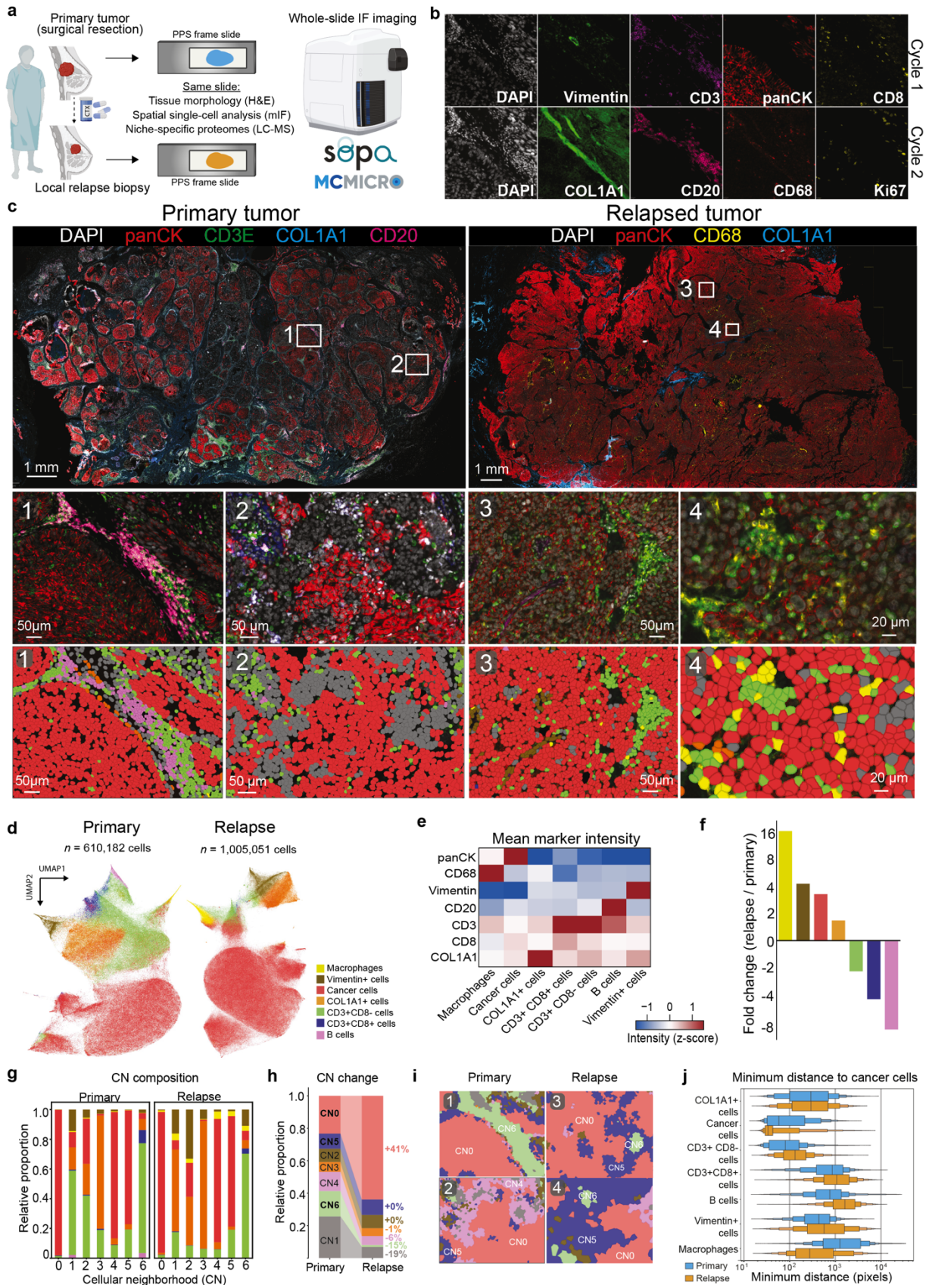

Fig. 4. Image acquisition and analysis of primary and recurrent triple-negative breast cancer (TNBC). **(a)** FFPE 5 µm sections from primary tumor and same-patient post-chemotherapy relapse sample were mounted on PPS frame slides. **(b)** Slides underwent multiplex immunofluorescence (mIF) staining and processing using MCMICRO pipeline with SOPA. **(c)** Whole-slide mIF images of samples with zoomed regions show overlaid cell phenotype information. **(d)** UMAP embeddings of segmented cells from each slide, based on morphology and marker intensity (excluding nuclear stains and background); unidentified cells excluded; n_neighbors = 25. **(e)** Heatmap of z-scored mean marker intensities across phenotyped cells. Phenotyping performed by thresholding markers per slide, rescaling intensities, and scimap phenotype function. **(f)** Fold change in cell type counts between recurrent and primary samples. **(g)** Relative composition of cellular neighborhoods per sample excluding unidentified cells. h) Selected regions with cellular neighborhoods overlaid. **(i)** Stacked bar plots showing cellular neighborhood frequency in each sample, calculated using scimap's spatialLDA function. **(j)** Boxen plots of minimum distance from cells to nearest cancer cell; each level of boxes corresponds to half the previous number of datapoints.

Cellular neighborhood guided proteomics delineates spatial tumor heterogeneity and putative molecular drivers of disease progression

We leveraged CN information to guide LMD sampling for exploratory proteomics (**Fig. 5a**) and selected CNs 0, 5, and 6, representing tumor, tumor-immune, and immune specific regions, respectively (**Suppl. Fig. 4**). For both samples, we distributed ROIs across tissue sections to assess spatial proteomic heterogeneity in a cell neighborhood resolved fashion. For CN0, we collected a single 25,000 µm2 contour per replicate. For smaller immune-enriched CN5 and CN6, we pooled proximate contours to normalize tissue input (**Fig. 5b**). In total, we collected 203 samples and processed them using our low-input tissue proteomics workflow. Using the Evosep One system with the 80 samples-per-day (SPD) Whisper Zoom method and timsTOF Ultra 2 mass spectrometer in diaPASEF mode, all samples were prepared and measured in less than one week. Using DIA-NN, we quantified 4,800 proteins for the tumor-specific CN0 and 3,500-4,000 for immune-enriched niches (**Suppl. Fig. 5a-b**). Proteomes showed CN-specific patterns, with 2,500 proteins quantified across all CNs, 750 unique to tumor-enriched and 250 unique to immune-enriched niches (**Fig. 5c**). Through SpatialData[15] integration and publicly available breast cancer scRNA-seq data [52], we confirmed that the tumor-specific CN0 showed epithelial cancer specific signatures, while immune-enriched CN6 featured strong T-cell signatures (**Fig. 5d**). As expected, the tumor-immune interface (CN5) showed signatures of both cell types. Principal component analysis revealed tissue-specific proteomes (PC1=29.3% variance) and spatial niche-specific profiles (PC2=17.3% variance) (**Fig. 5e-f**). Clustering of all proteomes identified three main clusters (**Fig. 5g**): Cluster 1 characterized the primary tumor-enriched CN0, enriched for protein transport and mitochondrial proteins; Cluster 2 featured proteins high in the relapse sample CN0,

showing high RNA processing and translation; and Cluster 3 proteins were abundant both in immune and tumor-immune CNs, featuring immune processes and extracellular matrix organization (**Fig. 5g, h**).

The strong proteomic differences in the tumor-specific CN, separating the primary and relapse sample, were intriguing (**Fig. 5d, g**), prompting further investigation in the context of spatial tissue organization. Overall, the DCIS proteome of the primary tumor showed higher heterogeneity compared to relapse sample, demonstrated by lower global proteome correlation (mean Pearson r = 0.91 versus 0.95, Mann-Whitney-U test p-value: 1.6E-46, **Fig. 5i**) and higher protein level variability (CV, **Suppl. Fig 5d**). Bootstrap analysis with 1000 resampling iterations across subset sizes showed that protein CVs plateaued at approximately 30 tumor ROIs and overall confirmed higher proteomic heterogeneity in the primary sample (**Suppl. Fig. 5c**). These results could be explained by clonal selection after chemotherapy, reducing clonal diversity and hence proteomic heterogeneity. Recent studies have identified spatial clonal niches in breast cancer tissues with distinct transcriptional and histological features [53,54]. We also found higher spatial autocorrelation values (Moran's I) in the DCIS-enriched primary tumor, indicating protein levels were more similar for neighboring tumor samples compared to distant ones (**Fig. 5j**).

To examine biological processes underlying chemoresistance and tumor progression in the relapse sample, we performed CN-guided pairwise proteomic comparisons. Both niches revealed pronounced quantitative differences (**Fig. 5k, m**). In the immune niche (CN6), pathway analysis identified interferon (IFN) gamma pathway as top upregulated in relapse, followed by complement/coagulation and heme metabolism (**Fig. 5l**). Consistent with imaging data showing CD68+ macrophage increase in relapse-associated immune niches (**Fig. 4f-g**), myeloid/macrophage gene expression programs were strongly enriched in the immune-niche specific proteome (**Suppl. Fig. 5e**). The relapse-associated tumor niche indicated a metabolic switch from oxidative phosphorylation to glycolysis, coinciding with higher EMT and MYC oncogenic programs (**Fig. 5n**), key features of chemoresistance and progressive disease [55,56]. These changes could be related to reduced oxygen and nutrient access in the core of the large relapse tumor. The interferon alpha pathway was the most upregulated pathway in the tumor-specific niche of relapse (**Fig. 5n**). Collectively, these niche-resolved data indicated both type I and II interferon signaling as overactive in relapse. Using SpatialData, we mapped the interferon pathway levels onto the IF image, which revealed that the IFN-high tumor-cell phenotype was present across

tissue section (**Fig. 5o**). The primary tumor instead showed high interferon alpha levels only in one central ROI. Notably, overactive IFN has been described as molecular driver of triple-negative inflammatory breast cancer (TN-IBC), a highly metastatic and chemoresistant subtype characterized by an immunosuppressive TME with high M1-like macrophages and reduced T lymphocyte infiltration compared to non-IBC [57]. These results were in excellent agreement with our data, suggesting that the relapse tumor represented TN-IBC.

In conclusion, our openDVP pipeline uncovered large-scale tissue microenvironmental and proteomic remodeling associated with tumor relapse and discovered tumor-intrinsic IFN signaling as a potential driver of chemoresistance and tumor progression in this patient [58].

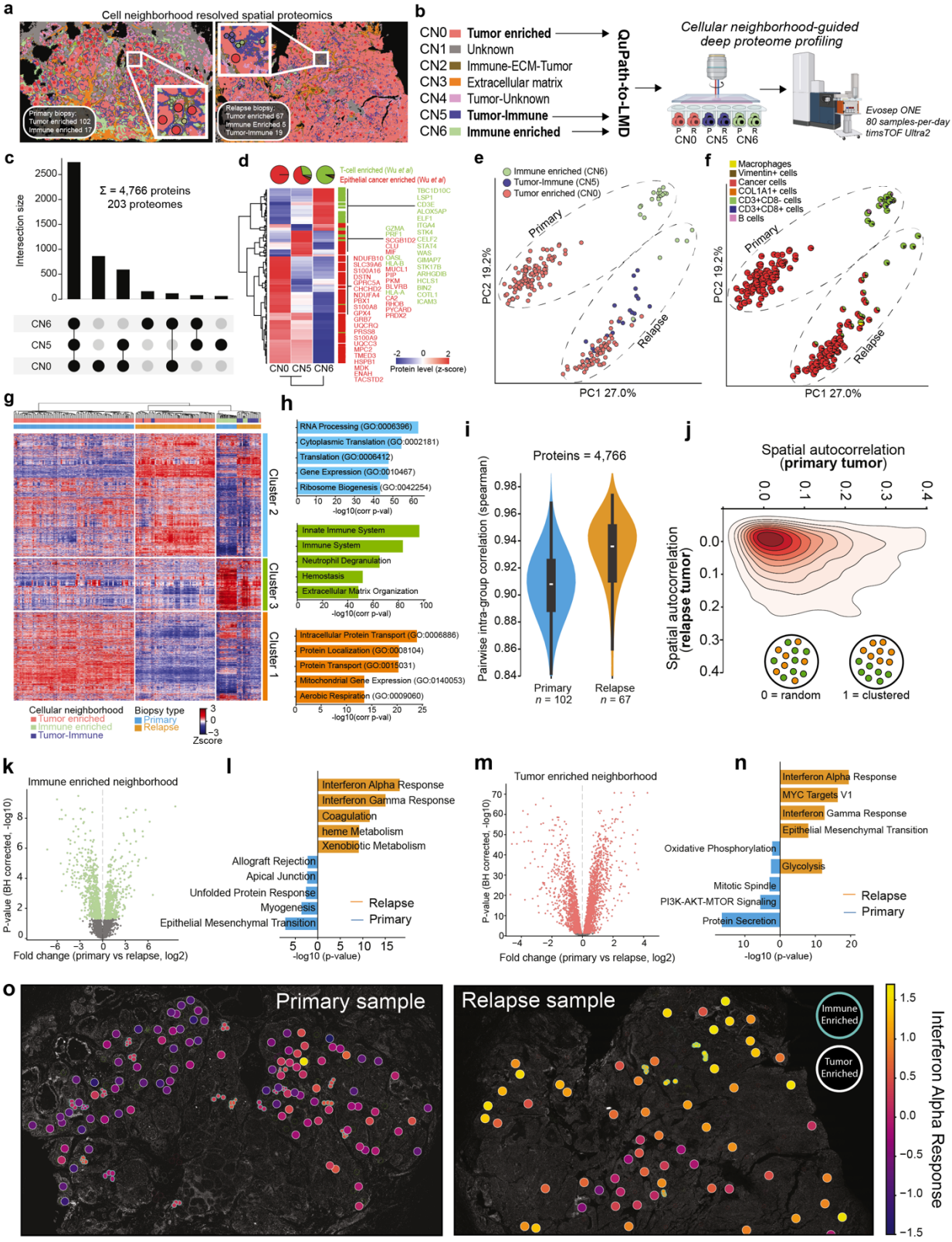

Figure 5. Spatial proteomic analysis of triple-negative breast cancer (TNBC) samples comparing primary and recurrent tumors. (a) Whole-slide overlay of cellular neighborhood (CN) annotations with contours for laser

microdissection-guided proteomics. Sample collection summaries are shown in boxes. **(b)** Three selected CNs for proteomics: Tumor Enriched, Immune Enriched, and Tumor-Immune. Regions were collected using laser microdissection and analyzed using a rapid (80 samples-per-day) LC-MS strategy. **(c)** UpSet plot showing protein identification overlap across CNs. **(d)** Heatmap showing signature markers from a recent RNAseq study [52]. Protein levels were z-scored, averaged per CN, and subjected to unsupervised hierarchical clustering. **(e)** Principal component analysis (PCA) of all samples, colored by CN. **(f)** PCA embedding with samples as pie charts reflecting cell phenotype proportions derived from image analysis. Note, both PCA plots show clustering by sample type (primary vs. relapse), followed by CN. **(g)** Heatmap displaying 4,570 proteins across 203 samples, clustered hierarchically (method: "average," distance metric: "cityblock"). Proteins filtered for 70% valid values in any CN group. **(h)** Protein clusters analyzed using EnrichR pathway enrichment using all identified proteins as background. **(i)** Violin plots showing pairwise intragroup correlations, highlighting greater proteomic variability in the primary tumor. **(j)** Density plot of Moran's I spatial autocorrelation for proteins across samples, showing greater spatial variability in the primary tissue. k) Volcano plot showing regulated proteins between immune-enriched CNs of primary and relapse tumors, FDR cut-off of 5%. **(l)** Barplot showing enriched MsigDB hallmarks between primary and relapse immune-enriched samples. **(m)** Volcano plot showing regulated proteins between tumor-enriched CNs of primary and relapse samples, FDR cut-off = 5%. **(n)** Barplot showing enriched MsigDB hallmarks between primary and relapse tumor enriched samples. **(o)** Overlay of interferon alpha response pathway (Hallmarks) showing z-scored pathway levels of tumor and immune-enriched samples. Note, the relapse sample featured consistently higher IFN levels across tissue.

Discussion

OpenDVP is the first Python-based framework for accessible and community-driven deep visual proteomics. Built on the scverse ecosystem, it supports FAIR principles by ensuring processed data are findable, accessible, interoperable, and reusable. Its modular design enables integration of tools for image segmentation, cell phenotyping, and spatial analysis through compatibility with platforms like MCMICRO, QuPath, and Napari. For broad accessibility, openDVP offers two workflow options: a simplified 'annotate-collect-measure' strategy (termed ‘flashDVP’) and an AI-powered pipeline optimized for high-performance computing and large image datasets. FlashDVP serves as a rapid spatial discovery platform based on manual sample annotation, particularly useful for the profiling of acellular regions like the extracellular matrix or cell types with more complex morphology, for which cell segmentation is more challenging. Applied to human placental tissue, we performed a comprehensive cell-type-resolved tissue proteomic analysis, identifying key proteins and pathways critical for placental biology. Additionally, in an aggressive lung cancer previously profiled by spatial transcriptomics in 3D, we confirmed differentially expressed genes and discovered additional niche-specific drug target candidates, highlighting the complementarity of multimodal spatial omics data.

The second workflow option represents an AI-powered DVP pipeline equipped with state-of-the-art tools for memory-efficient single cell and spatial analyses. Our breast cancer relapse study

showed how this pipeline performs accurate cell segmentation and neighborhood analyses to guide deep proteomic profiling. While single-cell laser microdissection provides highest biological granularity critical for single-cell applications [59] and mixed cell populations [60], this approach is generally more challenging due electrostatic forces, more difficult contour alignments, and potential cell-type admixing from imprecise laser microdissection. We therefore developed an alternative strategy that provides an excellent balance between biological resolution, efficiency and speed of tissue collection, and reproducibility of proteomic analysis. Instead of excising single cells, cellular neighborhood (CN)-guided proteome profiling represents a more robust and streamlined approach for phenotype-resolved discovery proteomics. Cellular neighborhoods combine cell phenotype and spatial information, offering a higher-level depiction of tissue architecture to pinpoint critical pathophysiological changes. As their proteomic profiles can be directly integrated with image-based phenotypes, this strategy allows for seamless cell-type deconvolution. We applied this approach to investigate the proteomic changes associated with tumor relapse in a triple-negative breast cancer patient. Based on multiplex immunofluorescence imaging, we uncovered substantial TME remodeling and quantitative proteomic changes between the primary and relapse tumor. We found that the primary DCIS-associated tumor featured higher intratumoral spatial proteomic heterogeneity compared to the more homogenous relapse sample, suggesting clonal selection associated with chemotherapy resistance and tumor recurrence. Our results further revealed elevated interferon signaling, EMT and glycolysis as dominant proteomic features of the relapse tumor, potentially targetable by JAK/STAT inhibitors or strategies to redirect glucose metabolism [38,61,62]. Looking ahead, we envision cellular neighborhood-guided proteome profiling particularly powerful in combination with higher plex DVP assays [63] (e.g., 20 - 30 markers), thereby significantly reducing the fraction of unknown phenotypes and providing much higher biological resolution to illuminate pathophysiological changes.

In conclusion, openDVP represents a significant advancement in making deep visual proteomics broadly accessible. Its open architecture provides a foundation for future innovations in spatial biology and serves as a platform for researchers as spatial discovery proteomics continues to evolve. While further progress in AI could enhance imaging and proteomic workflows for improved scalability, the adoption of openDVP across tissues and diseases could yield new biological insights, biomarkers, and drug targets. These efforts will also provide an important basis

for centralized spatial proteomics databases, integrating antibody and mass spectrometry-based data. We envision such community efforts to be essential for unlocking the full potential of spatial proteomics to transform our understanding of tissue biology in health and disease.

Acknowledgements

We thank our colleagues at the Max Delbrück Center (MDC) and Charité for their support and fruitful discussions. Furthermore, we acknowledge the MDC technology platform 'Proteomics' and 'Advanced light microscopy' for their great support. Gina Dörpholz, Pia Larsen and Jeannine Engel for administrative support and Janett König for laboratory support. Wouter-Michiel Vierdag for help with Napari plugin development and SpatialData. The authors also gratefully appreciate Martin Gauster (Medical University of Graz) and Andreas Glasner (Femina-Med) for patient recruitment collection of first-trimester human placental tissue (Medical University of Graz). J.N. and F.C. acknowledge funding support by the Federal Ministry of Education and Research (BMBF), as part of the National Research Initiatives for Mass Spectrometry in Systems Medicine, under grant agreement No. 161L0222. F.H. and F.C. were supported by Deutsche Forschungsgemeinschaft (HE 6249/5-3). This project received funding from the European Research Council (ERC) under the European Union's Horizon 2020 research and innovation program (grant agreement No. 101115681) and support by the ERC (ERC starting grant). S.Fl. was supported by grant 01ZX1917A from the Federal Ministry for Education and Research (BMBF) through the e:Med Initiative for Systems Medicine.

Author contributions

Conceptualization: J.N. and F.C.

Methodology: J.N., S.F., and M.T.

Resources: T.P., S.Fl., S.S., F.H., and F.K.

Experiments, J.N., S.F., and D.S.V.

Data curation: J.N., S.F., M.T., and D.S.V.

Data analysis: J.N., S.F., D.S.V., T.P., and F.C.

Figures: J.N., S.F., D.S.V., T.P., and F.C.

Supervision: J.N. and F.C.

Funding acquisition: N.R., F.H., and F.C.

Writing of the original draft: F.C. All authors have reviewed and edited the manuscript.

Declaration of interests

The authors declare that they have no competing interests.

Methods

Data availability

Mass spectrometry proteomics data have been deposited to the ProteomeXchange Consortium via the PRIDE partner repository [64]. RNA-seq data were obtained from GEPIA [39], an interactive web server for analyzing RNA sequencing expression data from the TCGA and GTEx projects, using a standard processing pipeline. The LUAD RNA-Seq dataset GEPIA used was based on the UCSC Xena project (http://xena.ucsc.edu).

Code availability

The source code of openDVP is fully opened and accessible on GitHub, including example tutorials: https://github.com/CosciaLab/openDVP, including the QuPath-to-LMD workflow https://github.com/CosciaLab/Qupath_to_LMD. The napari-cell-gater can be found at https://github.com/CosciaLab/napari-cell-gater.

Sample collection and patient cohort

Placenta samples

Placental tissue was collected from electively terminated pregnancies (gestational age, 7 – 11 weeks) with informed consent. Exclusion criteria were maternal age under 18 years, BMI >25 kg/m2, and maternal pathologies. Ethical approval was obtained from Medical University Graz Ethics Committee (31-019 ex18/19). After surgical extraction, tissue was stored at 4°C in culture medium (DMEM/F12 1:1, 1 g/dL glucose) and processed within 4 h. Villous tissue was rinsed in cold (4°C) 0.9% NaCl solution to remove blood, fixed with 10% formalin, paraffin embedded (FFPE), and dehydrated per standard protocols.

Lung cancer sample

We analyzed the primary tumor of a non-small cell lung cancer (NSCLC) patient. The patient, a 63-year-old woman with a 40 pack-year smoking history and no physical limitations (ECOG performance status 0), was diagnosed in March 2020 with a metabolically active tumor at the apex of the right upper lobe on positron emission tomography (PET) imaging. A transbronchial lung biopsy confirmed a TTF1-positive lung adenocarcinoma (LUAD) with acinar growth pattern. Two

months after diagnosis, the patient underwent right upper lobectomy. Gross examination was performed according to standardized protocols. The specimen was fixed in 10% buffered formalin and paraffin-embedded (FFPE). Histological examination, including diagnosis, tumor grading, pTNM classification, angioinvasion, lymphatic invasion, and tumor stage, was performed according to the 8th edition of the TNM classification (AJCC). Following diagnosis, the FFPE tissue block was stored at room temperature in the archive of the Institute of Pathology at the Charité University Hospital, Campus Mitte. The study was performed according to the ethical principles for medical research of the Declaration of Helsinki, and approval was approved by the Ethics Committee of the Charité University Medical Department in Berlin (EA4/243/21).

A comprehensive 3D spatial transcriptomic analysis of this tumor has been described recently based on 34 5-µm-thick consecutive sections (sections 4, 10, 16, 22, 28, and 34) [35] and a section-to-section distance of 30 µm. From the same tumor block, we profiled section 36 using proteomics after image registration in QuPath.

Triple negative breast cancer samples

Archival leftover diagnostic tissue from the tumor resection specimen and a specimen obtained two years later after relapse was selected from the archives of the Institute of Pathology, Charité Universitätsmedizin Berlin. At the time of diagnosis and primary resection, the patient had carcinoma in situ (DCIS), 38 mm in diameter, with multifocal stromal invasion. The multifocal invasive tumor had a total diameter of 9 mm, lacked expression of estrogen and progesterone receptors, and had an Her2-score of 1+, considered equivalent to a lack of HER2-gene amplification. The diagnosis was multifocal invasive triple-negative breast cancer (stage pT1b (m)). In 2022, the patient experienced a relapse with a diameter of 34 mm and ulceration of the skin (stage yrpT4b). The patient provided written consent for the use of leftover diagnostic material for research purposes. The project was approved by the IRB of Charité ("Ethics Committee"), project number EA1/253/19.

Immunofluorescence staining and imaging

Placenta tissue sections (5 µm) were mounted on metal frame PPS membrane slides, dried overnight, deparaffinized, and subjected to antigen retrieval in Tris/EDTA (pH 9) at 93 °C for 20 min. After cooling (20 min), slides were placed in warm distilled water (5 min) and cooled again

(5 min). Sections were washed with PBST (PBS + 0.1% Tween 20) and blocked with Ultra V Block (20 min, RT). For triple staining (CD163, CD31, E-cadherin), primary antibodies (Table 1) were diluted in PBST + 1% normal goat serum (NGS) and incubated overnight at 4°C. fter washing, secondary antibodies in PBST + 1% NGS (mouse IgG-AF647 and rabbit IgG-AF488, Table 1) were incubated for 1 h at RT in dark. Slides were washed and mounted with SlowFade Diamond containing DAPI. Rabbit immunoglobulin and mouse IgG controls showed no stains. Imaging was performed using Zeiss Axioscan 7. Cell phenotypes were manually annotated in QuPath following the flashDVP workflow (v0.4.2). Regions of interest (~50,000 μm²) were collected using Leica LMD7 (63x, brightfield) microscope into 384-well plates.

Cyclic immunofluorescence staining and imaging

Breast cancer tissue sections were incubated at 60 °C for 30 min and then deparaffinized and rehydrated (2x 5 min in Neo-Clear, 2x 2 min in 99% EtOH, 1x 2 min in 80% EtOH, 1x 2 min in 70% EtOH, 3x 1 min in 1x PBS). For decrosslinking, heat-mediated antigen retrieval was performed in pH 9 Tris buffer (Dako, #K800421-2, 1:50 in ddH_2O) in a steamer for 30min. Sections were washed in 1x PBS and pre-quenched in 4.5% H_2O_2 (in 25mM NaOH in PBS) for 2x 30 min. Cover glasses were mounted with 10% glycerol (in PBS) and the first image acquisition for background subtraction was performed using the Zeiss Axioscan 7 Slidescanner with a 20x/0.5NA objective at 2 × 2 binning. Slides were soaked in PBS for cover glass detachment for 5 min and then washed 3x 5 min in PBS to remove residual glycerol. Tissues were then blocked for 30 min in 3% BSA (in PBS, Serva #11948.01) at room temperature, followed by antibody staining in a humid chamber at 4 °C overnight. Antibodies are listed in the table below, all diluted 1:50 in the blocking buffer. The next day, sections were washed in PBS, mounted, and imaged with similar settings, while exposure times were adjusted to the fluorescent signal. Cover glasses were removed as before, sections were washed, and fluorescent signal was bleached as previously described for 30 min. For multiplexed immunofluorescence, tissue sections were washed 3x 5 min in PBS, and the second cycle of antibody staining was performed. Afterwards, sections were incubated for 3 min in hematoxylin, 10 min in tap water, dipped twice in ddH_2O, 30sec in eosin, dipped twice in ddH_2O, and dehydrated by dipping in increasing concentrations of EtOH (70-99%) for visible staining.

Antibody target protein	Vendor	Catalog no.	Clone	Fluorophore	Research resource identifier	Dilution
α-SMA	Abcam	ab184675	1A4	Alexa Fluor® 488	AB_2832195	1:50
CD3E	NovusBio	NBP2-54392AF647	C3e/1308	Alexa Fluor® 647	AB_3095415	1:50
CD8A	Thermo Fisher Scientific	53-0008-80	AMC908	Alexa Fluor® 488	AB_2574412	1:50
CD20	eBioscience	53-0202-80	L26	Alexa Fluor® 488	AB_10734357	1:50
CD68	CST	79594	D4B9C	PE	AB_2799935	1:50
E-cadherin	CST	3199	24E10	Alexa Fluor® 488	AB_10691457	1:50
Pan Cytokeratin	Thermo Fisher Scientific	41-9003-80	AE1/AE3	eFluor™ 570	AB_11218704	1:50
Vimentin	NovusBio	NBP1-97670AF750	V9	Alexa Fluor® 750	AB_10013743	1:50
COL1A1	NovusBio	NB600-408AF750	Polyclonal	Alexa Fluor® 750	AB_10000511	1:50
Ki67	CST	11882	D3B5	Alexa Fluor® 488	AB_2687824	1:50
CD163	Miltenyi	130-127-908	REA1309	PE	AB_2928274	1:50
E-cadherin	Cell Signalling	3195	24E10	-	AB_2291471	1:200
HLA-G	EXBIO	11-291-C100	MEM-G/1	-	AB_10734353	1:200
Anti-goat Ms IgG	Thermo Fisher Scientific	A21235	-	Alexa Fluor® 647	AB_2535804	1:1000
Anti-goat Rb IgG	Thermo Fisher Scientific	A11008	-	Alexa Fluor® 488	AB_143165	1:1000

Image analysis and contour export for laser microdissection

Triple negative breast cancer

Triple-negative breast cancer whole slide images were processed with MCMICRO: Tiles were illumination corrected with BASIC v1.1.1, then stitched and registered with ASHLAR v1.17.1. Channels were background-subtracted from autofluorescence images using Backsub v0.4.1. The image stack was processed using a modified SOPA snakemake pipeline. The nuclear signal from the first cycle was segmented using cellpose v2's "nuclei" model, with parameters: diameter 25, flow_threshold 0.8, cellprob_threshold –8, min_area 250, clip_limit 0.2, gaussian_sigma 1. For whole-slide images, we used SOPA's patchify function to tile images into 5000 pixels tall/wide squares with 100 pixel overlap to distribute segmentation tasks across HPC. Segmentation masks

were expanded by five pixels and used to quantify mean, standard deviation, and three quantiles (25% 50% 75%) of marker signal per cell. For quality control, image stacks were scaled to 8-bit and pyramidized with tile-size 4096. Analysis of quantified files applied these filtering steps with visual quality control: (1) removal of manually labelled artifact regions, (2) removal of cells with too low/high nuclear signal, (3) removal of cells with too small/large areas, (4) removal of dropout cells where DAPI ratio between first and last cycle was not between 0.15-1.05. Cell phenotyping used napari-cell-gater (github.com/CosciaLab/napari-cell-gater) to determine marker thresholds and scale marker signals for binomial distribution. Scimap's phenotype function with a phenotype-matrix labeled the cells. Manually labelled artifacts for one channel reduced signal for all cells in the annotation. For cellular neighborhood analysis, datasets were merged by concatenating adata objects, analyzed by scimap's spatial_lda function with knn=30 and k=7.

Laser microdissection and proteomic sample preparation

First trimester placenta

Samples were pooled at the bottom of each well with acetonitrile (2 × 10 µL) and vacuum-dried (30 min). Cell lysis was performed with 4 µL of 60 mM TEAB, followed by brief centrifugation (2,000 RCF, 1 min) and heating at 95 °C for 60 min in a Bio-Rad thermal cycler (384-well module, lid at 110 °C). ACN (1 µL; 20% final) was added, and the samples were incubated at 75 °C for 60 min. After cooling, 2 µL LysC (2 ng/µL in LC-MS grade H_2O) was added and digestion was performed at 37 °C for 4 h. Trypsin (2 µL, 2 ng/µL; Promega Trypsin Gold) was added for overnight digestion at 37 °C. Digestion was stopped with 1% TFA (v/v), and samples were vacuum-dried (~60 min, 60 °C) and stored at –20 °C. Before LC-MS, 4.2 µL MS loading buffer (3% ACN, 0.2% TFA) was added; the plate was vortexed (10 s), centrifuged (5 min, 2,000 RCF) and 4µL injected into the EASY-nLC-1200 system.

Triple negative breast cancer

For laser microdissection, slides were stained with H&E on PPS-Membrane Frame Slides. A total of 210 annotations were made in QuPath with a cellular neighborhood overlay. The total sample area for each sample was 25,000 µm2. We used the Leica LMD 7 system with Leica Laser Microdissection software v. 8.3.0.08259. Tissue was collected using the 20x objective (HC PL FL L 20x/0.40 CORR) in brightfield with laser settings: power 55, aperture 1, speed 20, middle pulse

count 1, final pulse –1, Head current 35-45% (adjusted based on tissue thickness), pulse frequency ~2000. Contours were collected in low-binding 384-well plates (Eppendorf 0030129547). To ensure tissue settling at the bottom of wells, 20µL of acetonitrile was added, followed by vortexing and vacuum drying for 10 min at 60 °C. Wells were inspected to confirm collection. Protein extraction and digestion used a DDM-based protocol. A lysis buffer containing 0.025% DDM, 5 mM TCEP, 20 mM CAA, and 0.1 M TEAB in water was dispensed into wells (4 µL per sample) using a MANTIS Liquid Dispenser. Plates were sealed with PCR ComfortLid seals and incubated at 95 °C for 60 min. After cooling, 2µL of LysC (4 ng/µL in 0.1 M TEAB [pH 8.5] with 30% acetonitrile) was added, and samples were digested for 4 h at 37 °C in a thermal cycler. Subsequently, 3µL of trypsin (2ng/µL in 0.1 M TEAB [pH 8.5] with 10% acetonitrile) was added, and digestion proceeded overnight at 37 °C. Samples were vacuum dried for peptide cleanup. Peptides were purified using Evotips (Evosep) following manufacturer's instructions, and samples were kept with Buffer A until measurement.

Liquid chromatography and mass spectrometry (LC-MS)

First trimester placenta

Peptides were analyzed using an EASY-nLC 1200 (Thermo Fisher) coupled to a trapped ion mobility spectrometry quadrupole time-of-flight mass spectrometer (timsTOF SCP, Bruker Daltonik) with a CaptiveSpray nano-electrospray source. Samples were loaded onto a 20 cm in-house packed C18 column (75 µm ID, 1.9 µm ReproSilPur C18-AQ silica beads, Dr. Maisch, Germany) and separated at 250 nL/min with a gradient of increasing concentrations of buffer B (0.1% formic acid, 90% ACN in LC-MS grade H2O) to 60% buffer A (3% ACN, 0.1% formic acid in LC-MS grade H2O). The gradient duration was 21 min, and the column temperature was maintained at 40 °C. MS acquisition was performed in diaPASEF mode with a 1.8 s cycle time. Ion accumulation and ramp times in the dual TIMS analyzer were 100 ms each; the ion mobility range was $1/K_0$ = 1.6–0.6 Vs cm^{-2} and the m/z range 100–1,700. The collision energy decreased linearly from 59 eV ($1/K_0$ = 1.6) to 20 eV ($1/K_0$ = 0.6). Singly charged precursors were excluded using a polygon filter (timsControl, Bruker).

Triple negative breast cancer

Liquid chromatography was performed using the Evosep One LC system connected to a trapped ion mobility spectrometer with a quadrupole time-of-flight mass spectrometer (timsTOF Ultra, Bruker Daltonik). Separation was performed using an Evosep 80SPD gradient with an IonOpticks Aurora Rapid column. The solvents were Buffer A (LC-MS grade water with 0.1% formic acid) and Buffer B (acetonitrile with 0.1% formic acid). Samples were measured in dia-PASEF acquisition mode. DIA-NN (version 1.9) analyzed the dia-PASEF raw data and generated spectral libraries. A human reference proteome FASTA file (UniProt, release 2022, UP000005640_9606) was downloaded on April 8, 2022, and supplemented with common contaminants. In silico libraries were generated using deep learning predictions of MS/MS spectra, retention times (RT), and ion mobilities (IM) across a 300–1200 m/z range. Fixed modifications included N-terminal methionine excision and cysteine carbamidomethylation. Digestion settings allowed up to two missed cleavages, with precursor charge states restricted to 2–4. DIA-NN was executed in default mode with adjustments: MS1 and MS2 mass accuracies set to 15.0 ppm, scan windows assigned automatically (set to 0), and isotopologue detection enabled. Settings included match-between-runs, heuristic protein inference (restricted to gene-level annotation), and exclusion of shared spectra. The neural network classifier ran in single-pass mode. Quantification used the QuantUMS strategy, cross-run normalization was RT-dependent, and spectral library generation used smart profiling.

Proteomic data analysis

First trimester placenta

Raw data were acquired using timsControl (v3.1, Bruker) and processed in DIA-NN (v1.8.1) in library-free mode using a predicted human spectral library (UniProt, 2021). Default settings were used with adjustments: mass range 100–1,700 m/z, precursor charge states 2–4, max 2 miscleavages, MS1/MS2 mass accuracy 15 ppm, match-between-runs enabled, and quantification set to 'Robust LC'. Protein-level outputs (pg_matrix.tsv and unique_genes_matrix.tsv) were analysed in Perseus [65](v.1.16.0.5). Missing values were imputed from a normal distribution (width = 0.3, downshift = 1.8) after filtering for ≥70% quantified values per cell type group. Matrices were further analyzed in R (v4.1.2). To identify phenotype-specific protein markers, highly variable proteins were selected based on an ANOVA F-values greater than four. Differential

abundance was assessed using Welch's two-sided t-test followed by Benjamini–Hochberg FDR correction. Identified marker proteins (FDR < 0.05) overlapping with public transcriptomic datasets were visualized using DiVenn [66].

Receptor ligand communication analysis was done using CellChat and included receptors and ligands indexed as "secreted," "cell-cell contact" or "ECM-receptor" in their database. We used standard parameters (excluding per-protein smoothing) of 1000 permutations for the probabilistic inference of each cell pair and transmitter-receiver interaction, considering heterometric structures and interactor mediator proteins.

Triple negative breast cancer

Proteomic data analysis was performed in Python v3.12.8, using AnnData v0.11.2 and SpatialData v0.4.0 as the main data formats. Analysis was performed using opendvp functions with geopandas v1.0.1 and pandas v2.2.3 in the background. Plotting was performed using matplotlib v3.10.0, seaborn v0.13.2, and pycomplexheatmap. The DIA-NN output was processed and adapted to the AnnData object using the opendvp.DIANN_to_adata function, and quality control samples were filtered out. Proteins that did not have at least 70% valid values in any cellular neighborhood were filtered out. The remaining NaN values were imputed by low-abundance normal distribution per protein (width=0.3, downshift=1.8). Scanpy v1.11.0 was used to perform PCA dimensionality reduction and plotting. Hierarchical clustering and plotting of heatmap took place with pycomplexheatmap v1.8.1, using method "average," and metric "cityblock." T-tests and ANOVA were performed using pingouin v0.5.5. Spearman's correlation was calculated using scipy v1.16.

Declaration of generative AI and AI-assisted technologies in the writing process

During the preparation of this manuscript, the authors used Paperpal to improve the readability and language of the text. After using this tool, the authors reviewed and edited the content as needed and take full responsibility for the content of the publication

Supplementary Figures

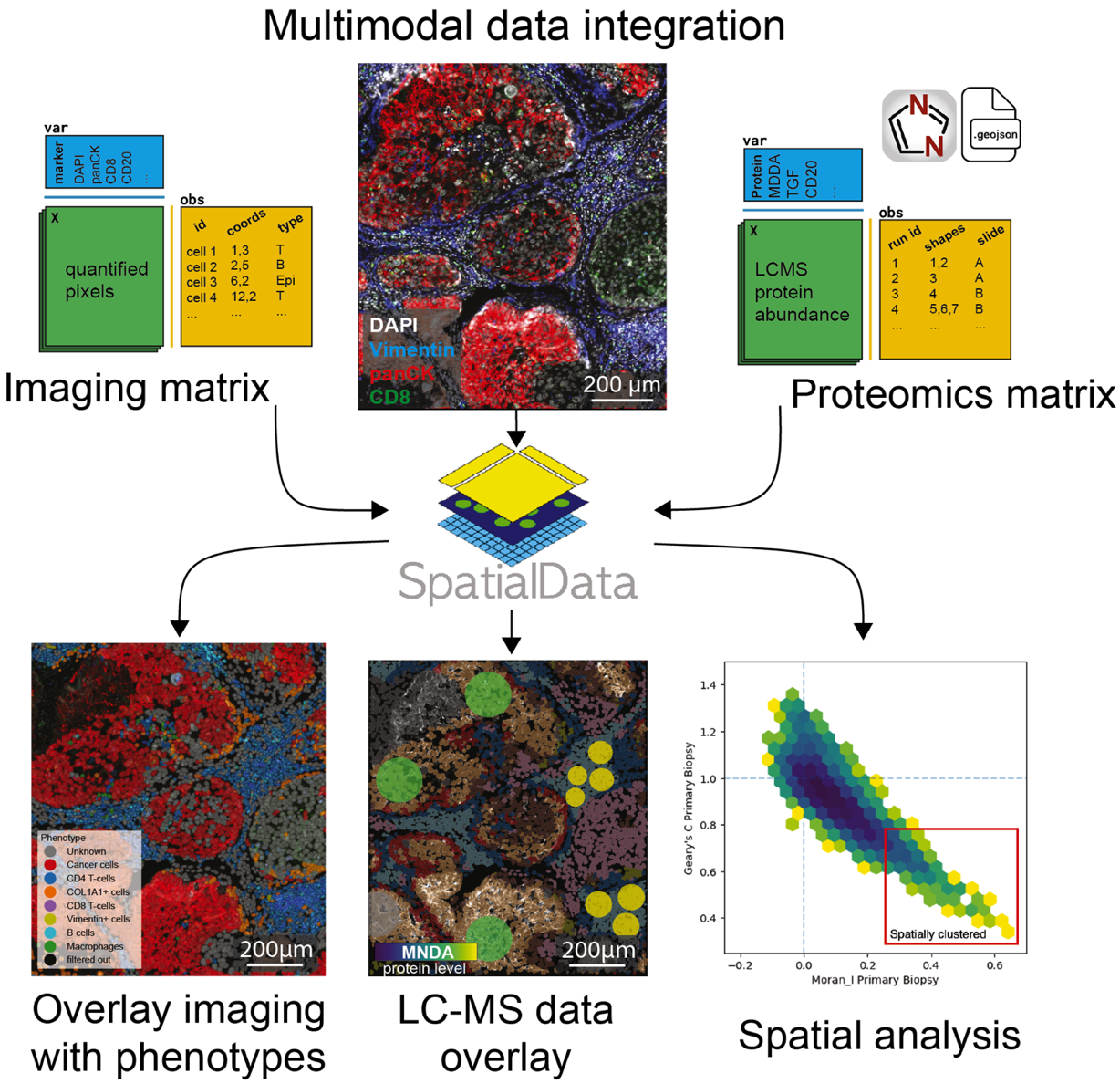

Supplementary Fig. 1, related to Fig 1.
Diagram showing how openDVP harnesses the scverse's SpatialData data format to integrate antibody-based imaging, the image analysis matrix, and LC-MS-based spatial proteomics. This allows users to overlay various information layers to best guide laser microdissection and spatial proteomics analysis.

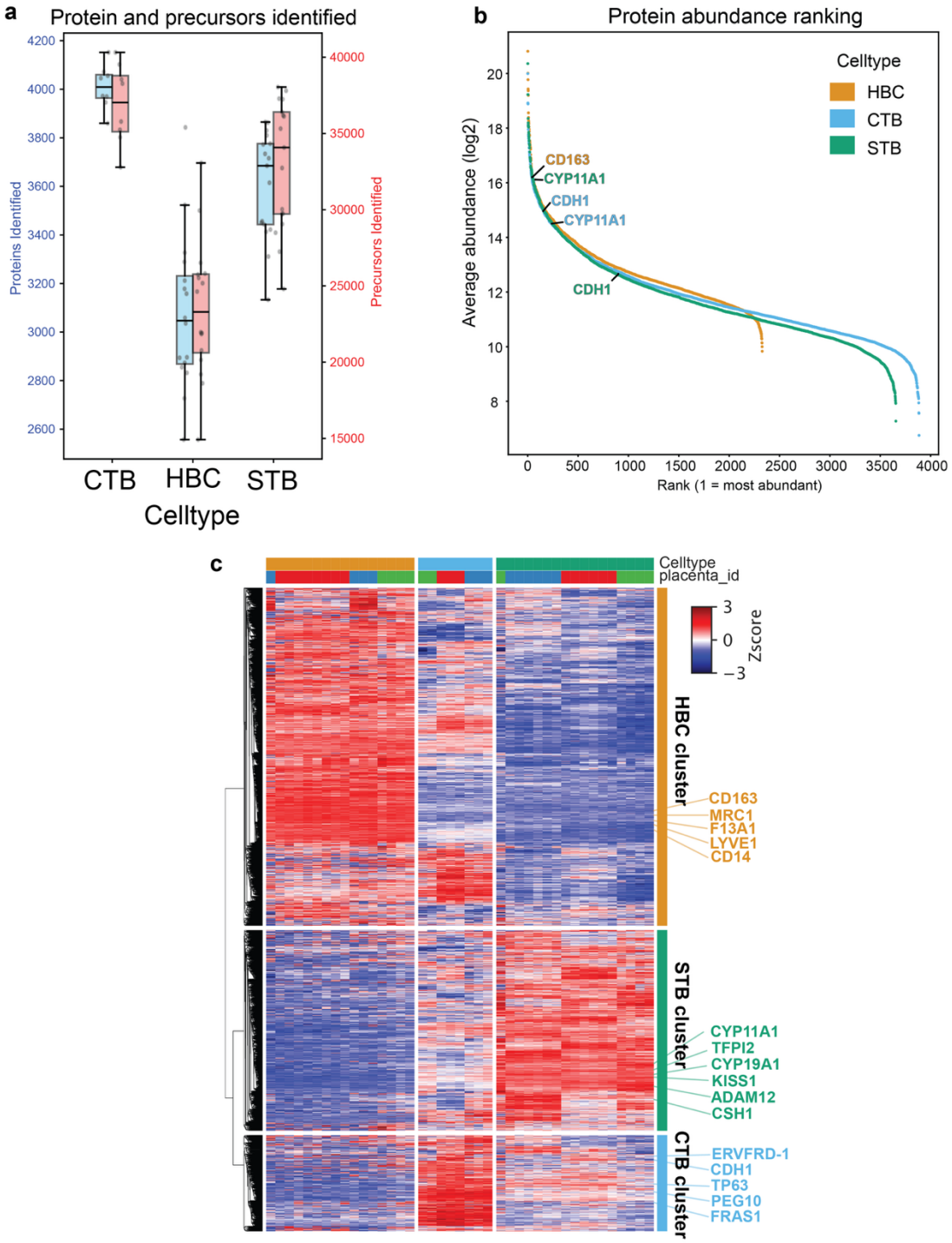

Supplementary Fig. 2, related to Fig. 2. (a) Box plots showing the number of proteins (blue) and precursors (pink) identified per cell type; each dot represents a sample. **(b)** Rankplot showing the dynamic range of proteins measured with labelled canonical markers and their rank for each cell type. **(c)** Unsupervised hierarchical clustering of 3,994 proteins, showing three distinct cell-type specific protein clusters used in **Fig. 2h.** Canonical markers of each cell type are labelled. The metric for clustering is "cityblock," and the mode is "average." Clustering was performed by splitting the dendrogram into three largest groups. CTB, cytotrophoblast; STB, syncytiotrophoblast; HBC, Hofbauer cell.

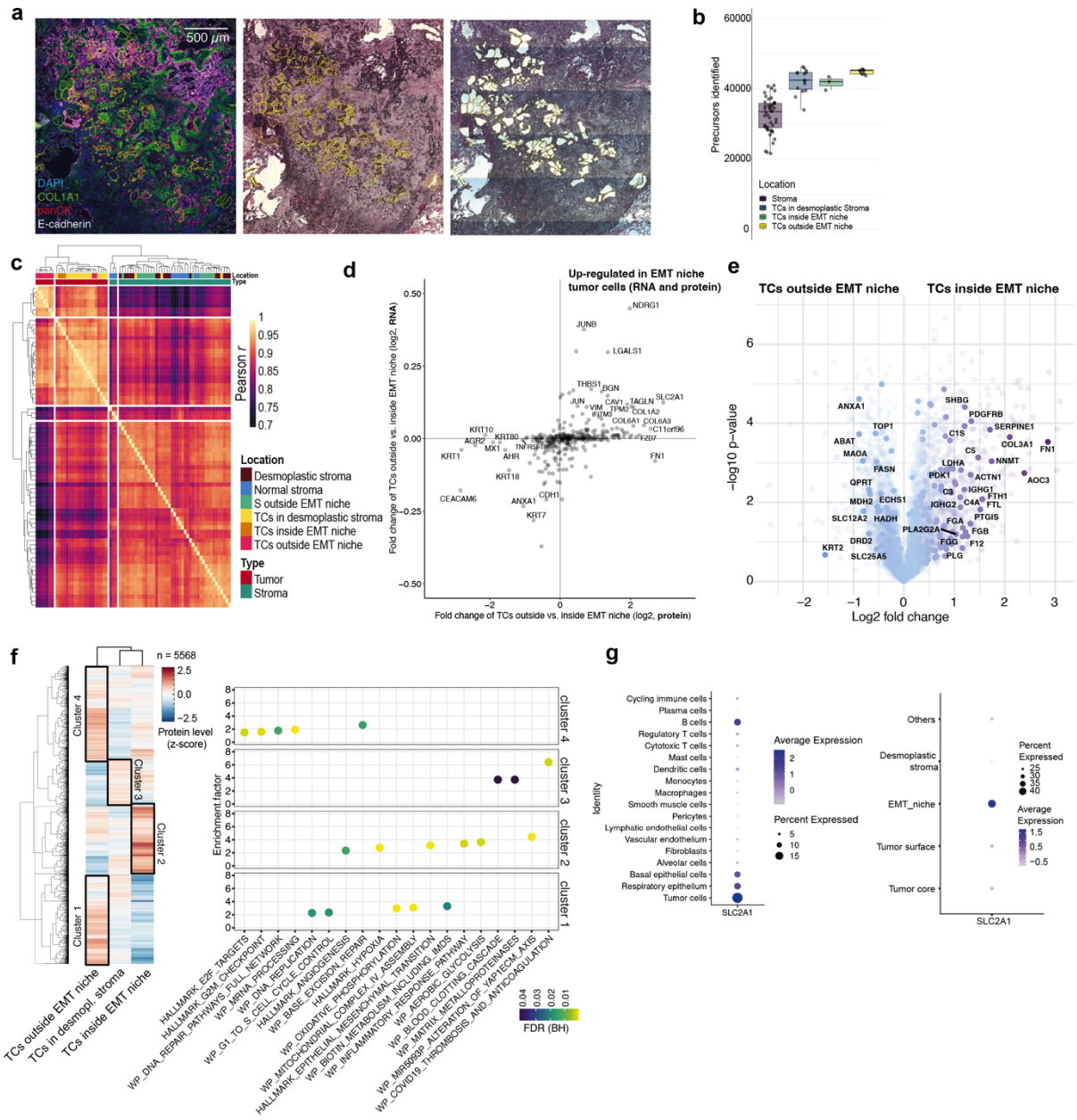

Supplementary Fig. 3, related to Fig. 3. **(a)** Imaging modalities (H&E and IF) used to guide laser microdissection. Yellow annotations show ROIs used for proteomic profiling. Left: Multiplex immunofluorescence used to locate tumor and stromal niches identified by spatial transcriptomics. H&E staining showing ROIs before (middle panel) and after LMD collection (right panel). **(b)** Boxplot showing the number of identified precursors per sample type. **(c)** Pearson's correlation heatmap for all analyzed samples. **(d)** Scatterplot comparing fold changes between tumor cells inside and outside the EMT niche, for both spatial proteomics and spatial transcriptomics. **(e)** Volcano plot showing differentially abundant proteins between tumor cells inside and outside the EMT niche as defined by CosMx spatial transcriptomics. **(f)** Heatmap showing clusters of proteins between tumor cells inside the EMT niche, outside the EMT niche, and in the desmoplastic stroma. The dot plot shows enriched Hallmarks and WikiPathways pathways for the different clusters using ClusterProfiler R package [67]. **(g)** Dot plot of SLC2A1 expression across all cell types (left) and in tumor cells distributed in different niches (right). Dot size indicates the percentage of gene-expressing cells; color represents average expression (log-normalized and scaled).

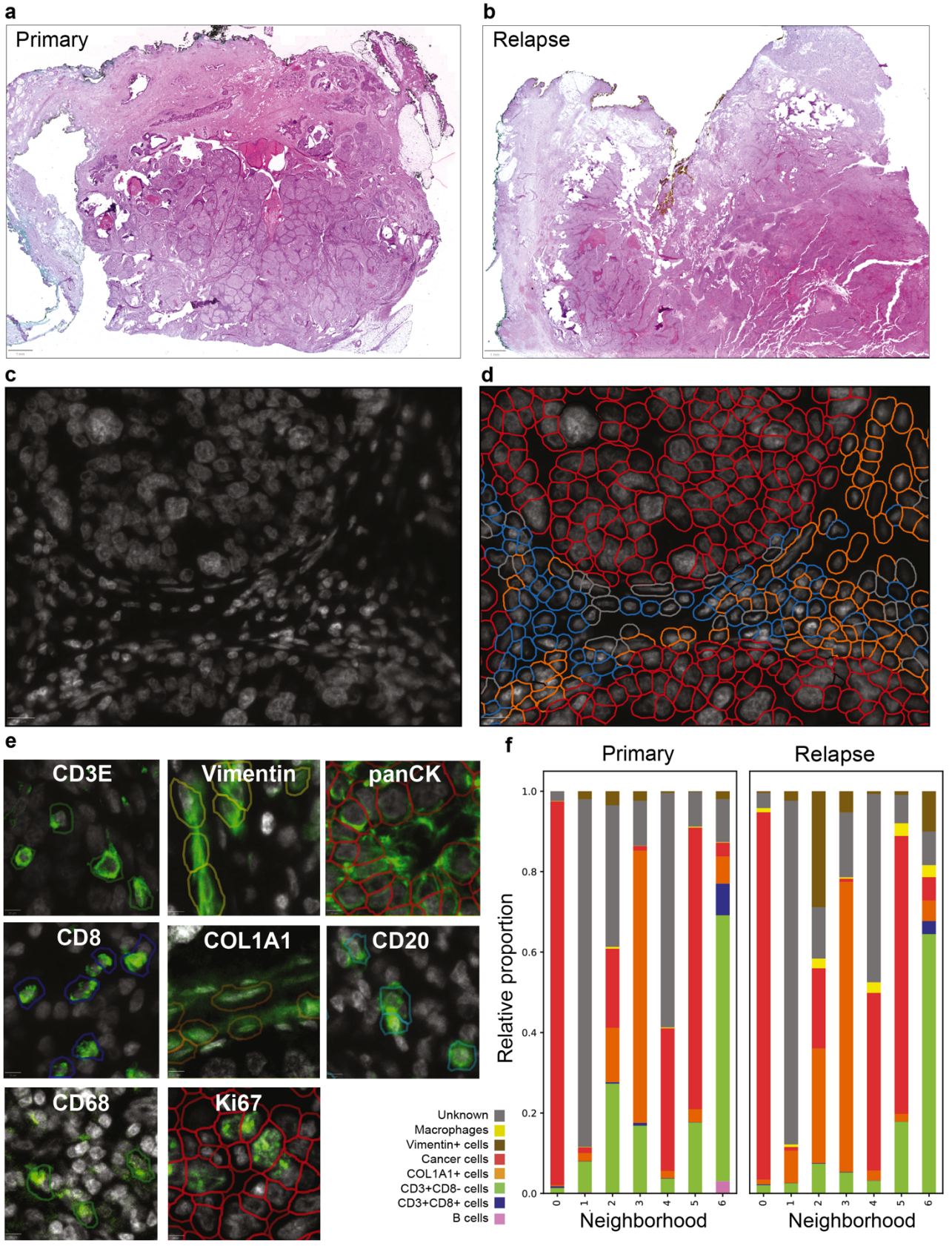

Supplementary Fig. 4, related to Fig. 4. **(a)** H&E image of the primary tissue. **(b)** H&E image of the relapse tissue. Both tissues showed minor tissue losses due to cyclic imaging on PPS frame slides. **(c)** Zoom-in of the primary tissue. The white color shows DAPI as the nuclear counterstain. **(d)** Segmentation masks coloured by assigned phenotype labels. **(e)** Exemplary images for each IF marker used, overlaid with segmentation mask. Colors represent phenotyped cells for each marker (not for Ki67). **(f)** Barplots with cellular neighborhood compositions for each sample, showing the proportion of unclassified cells in grey. Related to Fig. 4g.

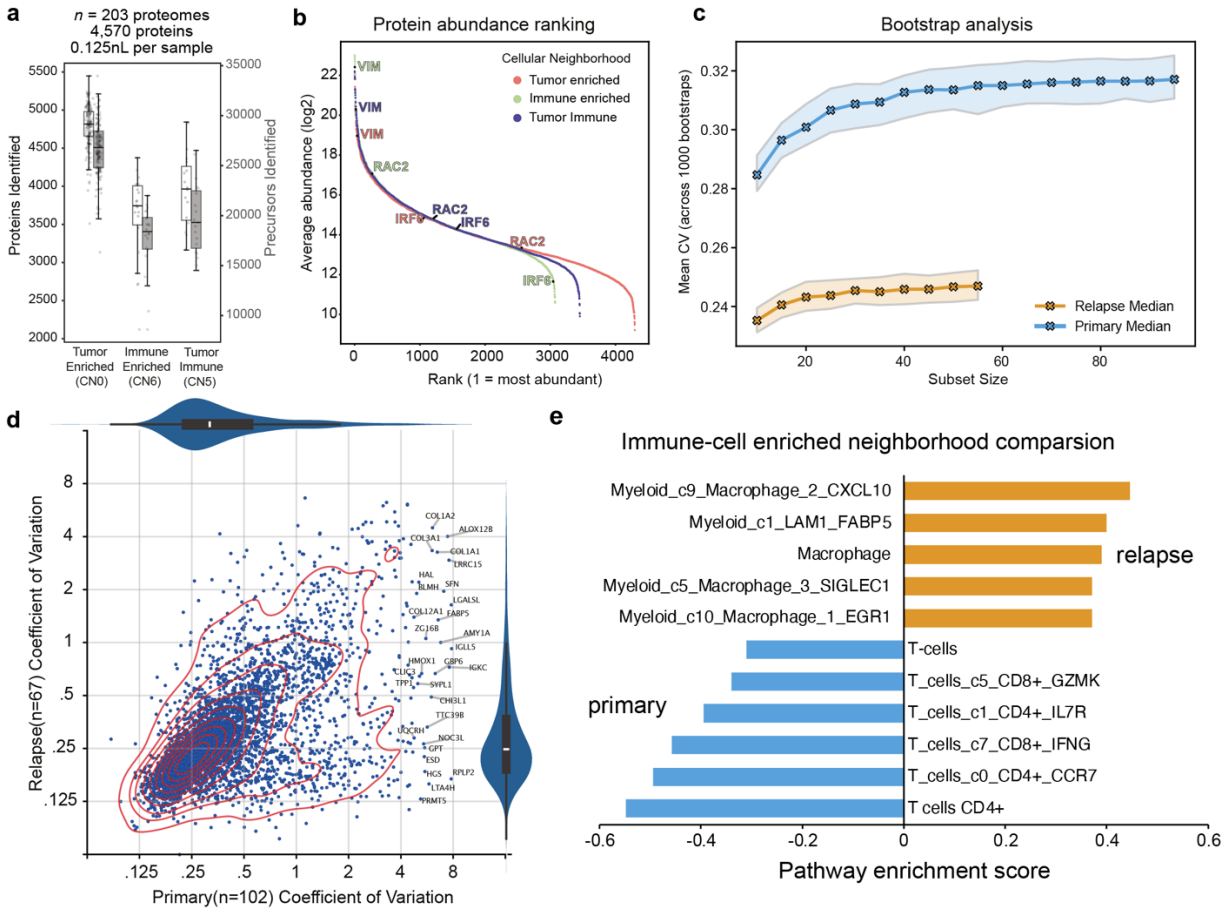

Supplementary Fig. 5, related to Fig. 5. (a) Boxplot showing proteins and precursors identified per group of cellular neighborhoods. **(b)** Rankplot showing the dynamic range of protein abundance for each neighborhood. Vimentin (VIM) and RAC2 show the highest abundance in the immune-enriched samples, and IRF6 in tumor-enriched samples. **(c)** Line plot showing the spread of the mean CV of 1000 bootstrap simulations, repeated across different subset sizes for both samples. Note, plateauing was observed around 30-40 samples. **(d)** Scatterplot of intra-tissue protein level variability (CV) comparing the primary and relapse sample. Only samples of the tumor-specific CN0 were used analysis. Note, the primary tumor showed overall higher proteome variability. **(e)** Barplot of enriched cell type signatures between the primary and relapse sample. Only samples of the immune enriched CN6 were used for analysis. Breast cancer-specific cell type signatures were obtained from publicly available scRNAseq data described in Wu *et al*. [52]. Note, the primary sample showed higher T cell signatures (e.g., CD4+, CD8+), whereas the relapsed immune niche featured higher myeloid/macrophage scores.

References

1. Bressan, D., Battistoni, G. & Hannon, G. J. The dawn of spatial omics. *Science (1979)* **381**, 1–35 (2023).
2. Method of the Year 2024: spatial proteomics. *Nat Methods* **21**, 2195–2196 (2024).
3. de Souza, N., Zhao, S. & Bodenmiller, B. Multiplex protein imaging in tumour biology. *Nat Rev Cancer* **24**, 171–191 (2024).
4. Lewis, S. M. *et al.* Spatial omics and multiplexed imaging to explore cancer biology. *Nat Methods* **18**, 997–1012 (2021).
5. Aebersold, R. & Mann, M. Mass-spectrometric exploration of proteome structure and function. *Nature* vol. 537 347–355 Preprint at https://doi.org/10.1038/nature19949 (2016).
6. Horvath, P. & Coscia, F. Spatial proteomics in translational and clinical research. *Molecular Systems Biology* 1–5 (2025) doi:10.1038/s44320-025-00101-9.
7. Mund, A., Brunner, A.-D. & Mann, M. Unbiased spatial proteomics with single-cell resolution in tissues. *Mol Cell* **82**, 2335–2349 (2022).
8. Mund, A. *et al.* Deep Visual Proteomics defines single-cell identity and heterogeneity. *Nature Biotechnology 2022* 1–10 (2022) doi:10.1038/s41587-022-01302-5.
9. Nordmann, T. M. *et al. Spatial Proteomics Identifies JAKi as Treatment for a Lethal Skin Disease*. *Nature* vol. 635 (Springer US, 2024).
10. Rosenberger, F. A. *et al.* Deep Visual Proteomics maps proteotoxicity in a genetic liver disease. *Nature 2025 642:8067* **642**, 484–491 (2025).
11. Schapiro, D. *et al.* MCMICRO: a scalable, modular image-processing pipeline for multiplexed tissue imaging. *Nat Methods* **19**, 311–315 (2022).
12. Blampey, Q. *et al.* Sopa: a technology-invariant pipeline for analyses of image-based spatial omics. *Nat Commun* **15**, (2024).
13. Bankhead, P. *et al.* QuPath: Open source software for digital pathology image analysis. *Scientific Reports 2017 7:1* **7**, 1–7 (2017).
14. Chiu, C.-L., Clack, N. & community, the napari. napari: a Python Multi-Dimensional Image Viewer Platform for the Research Community. *Microscopy and Microanalysis* **28**, 1576–1577 (2022).
15. Marconato, L. *et al.* SpatialData: an open and universal data framework for spatial omics. *Nature Methods 2024* 1–5 (2024) doi:10.1038/s41592-024-02212-x.
16. DI Tommaso, P. *et al.* Nextflow enables reproducible computational workflows. *Nat Biotechnol* **35**, 316–319 (2017).
17. Köster, J. *et al.* Sustainable data analysis with Snakemake. *F1000Res* **10**, (2021).
18. Nirmal, A. J. & Sorger, P. K. SCIMAP: A Python Toolkit for Integrated Spatial Analysis of Multiplexed Imaging Data. *J Open Source Softw* **9**, 6604 (2024).
19. Wolf, F. A., Angerer, P. & Theis, F. J. SCANPY: Large-scale single-cell gene expression data analysis. *Genome Biol* **19**, 1–5 (2018).

20. Meyer-Bender, M. *et al.* Spatialproteomics - an interoperable toolbox for analyzing highly multiplexed fluorescence image data. 1–26 (2025).
21. Regev, A. The Human Cell Atlas -Slides. *Elife* **6**, e27041 (2017).
22. Rajewsky, N. *et al.* LifeTime and improving European healthcare through cell-based interceptive medicine. *Nature* **587**, 377–386 (2020).
23. Burton, G. J. & Fowden, A. L. The placenta: A multifaceted, transient organ. *Philosophical Transactions of the Royal Society B: Biological Sciences* **370**, (2015).
24. Bezemer, R. E., Faas, M. M., van Goor, H., Gordijn, S. J. & Prins, J. R. Decidual macrophages and Hofbauer cells in fetal growth restriction. *Front Immunol* **15**, 1379537 (2024).
25. Makhmut, A. *et al.* A framework for ultra-low-input spatial tissue proteomics. *Cell Syst* **14**, 1002-1014.e5 (2023).
26. Demichev, V., Messner, C. B., Vernardis, S. I., Lilley, K. S. & Ralser, M. DIA-NN: neural networks and interference correction enable deep proteome coverage in high throughput. *Nat Methods* **17**, 41–44 (2020).
27. Gonzalez, T. L. *et al.* Sex differences in the late first trimester human placenta transcriptome. *Biol Sex Differ* **9**, (2018).
28. Nonn, O. *et al.* Senescent Syncytiotrophoblast Secretion During Early Onset Preeclampsia. *Hypertension* **82**, (2024).
29. Baczyk, D., Drewlo, S. & Kingdom, J. C. P. Emerging role of SUMOylation in placental pathology. *Placenta* **34**, 606–612 (2013).
30. Baczyk, D., Audette, M. C., Coyaud, E., Raught, B. & Kingdom, J. C. Spatiotemporal distribution of small ubiquitin-like modifiers during human placental development and in response to oxidative and inflammatory stress. *Journal of Physiology* **596**, 1587–1600 (2018).
31. Ruano, C. S. M. *et al.* Alternative splicing in normal and pathological human placentas is correlated to genetic variants. *Hum Genet* **140**, 827–848 (2021).
32. Turco, M. Y. & Moffett, A. Development of the human placenta. *Development (Cambridge)* **146**, (2019).
33. Reese, J. A. *et al.* Platelet Counts during Pregnancy. *New England Journal of Medicine* **379**, 32–43 (2018).
34. Jin, S. *et al.* Inference and analysis of cell-cell communication using CellChat. *Nat Commun* **12**, 1–20 (2021).
35. Tancredi Massimo Pentimalli, A. *et al.* Combining spatial transcriptomics and ECM imaging in 3D for mapping cellular interactions in the tumor microenvironment. *Cell Syst* **0**, 101261 (2025).
36. David, M. *et al.* Durable responses to imatinib in patients with PDGFRB fusion gene–positive and BCR-ABL–negative chronic myeloproliferative disorders. *Blood* **109**, 61–64 (2007).

37. Stine, Z. E., Schug, Z. T., Salvino, J. M. & Dang, C. V. Targeting cancer metabolism in the era of precision oncology. *Nat Rev Drug Discov* **21**, 141–162 (2022).
38. Ligorio, F. *et al.* Early downmodulation of tumor glycolysis predicts response to fasting-mimicking diet in triple-negative breast cancer patients. *Cell Metab* **37**, 330-344.e7 (2025).
39. Tang, Z. *et al.* GEPIA: A web server for cancer and normal gene expression profiling and interactive analyses. *Nucleic Acids Res* **45**, W98–W102 (2017).
40. Goldman, M. J. *et al.* Visualizing and interpreting cancer genomics data via the Xena platform. *Nature Biotechnology 2020 38:6* **38**, 675–678 (2020).
41. Uhlen, M. *et al.* A pathology atlas of the human cancer transcriptome. *Science (1979)* **357**, (2017).
42. Liu, Y. *et al.* Conserved spatial subtypes and cellular neighborhoods of cancer-associated fibroblasts revealed by single-cell spatial multi-omics. *Cancer Cell* **43**, 905-924.e6 (2025).
43. Ma, C. *et al.* Pan-cancer spatially resolved single-cell analysis reveals the crosstalk between cancer-associated fibroblasts and tumor microenvironment. *Mol Cancer* **22**, 170 (2023).
44. Barkley, D. *et al.* Cancer cell states recur across tumor types and form specific interactions with the tumor microenvironment. *Nature Genetics 2022 54:8* **54**, 1192–1201 (2022).
45. Bianchini, G., De Angelis, C., Licata, L. & Gianni, L. Treatment landscape of triple-negative breast cancer — expanded options, evolving needs. *Nat Rev Clin Oncol* **19**, 91–113 (2022).
46. Jackson, H. W. *et al.* The single-cell pathology landscape of breast cancer. *Nature* **578**, 615–620 (2020).
47. Ranek, J. S. *et al.* QUICHE reveals structural definitions of anti-tumor responses in triple negative breast cancer. (2025).
48. Miroshnychenko, D. *et al.* Stroma-Mediated Breast Cancer Cell Proliferation Indirectly Drives Chemoresistance by Accelerating Tumor Recovery between Chemotherapy Cycles. *Cancer Res* **83**, 3681–3692 (2023).
49. Wang, X. Q. *et al.* Spatial predictors of immunotherapy response in triple-negative breast cancer. *Nature* **621**, 868–876 (2023).
50. de Visser, K. E. & Joyce, J. A. The evolving tumor microenvironment: From cancer initiation to metastatic outgrowth. *Cancer Cell* **41**, 374–403 (2023).
51. Friedman-DeLuca, M., Karagiannis, G. S., Condeelis, J. S., Oktay, M. H. & Entenberg, D. Macrophages in tumor cell migration and metastasis. *Front Immunol* **15**, 1–16 (2024).
52. Wu, S. Z. *et al.* A single-cell and spatially resolved atlas of human breast cancers. *Nat Genet* **53**, 1334–1347 (2021).
53. Lomakin, A. *et al.* Spatial genomics maps the structure, nature and evolution of cancer clones. *Nature* **611**, 594–602 (2022).

54. Casasent, A. K. *et al.* Multiclonal Invasion in Breast Tumors Identified by Topographic Single Cell Sequencing Article Multiclonal Invasion in Breast Tumors Identified by Topographic Single Cell Sequencing. *Cell* **172**, 205-210.e12.
55. Pavlova, N. N. & Thompson, C. B. The Emerging Hallmarks of Cancer Metabolism. *Cell Metabolism* vol. 23 27–47 Preprint at https://doi.org/10.1016/j.cmet.2015.12.006 (2016).
56. Hanahan, D. & Weinberg, R. A. Hallmarks of cancer: The next generation. *Cell* vol. 144 646–674 Preprint at https://doi.org/10.1016/j.cell.2011.02.013 (2011).
57. Wang, X. *et al.* Genomic and transcriptomic analyses identify distinctive features of triple-negative inflammatory breast cancer. *NPJ Precis Oncol* **8**, 1–14 (2024).
58. Benci, J. L. *et al.* Tumor Interferon Signaling Regulates a Multigenic Resistance Program to Immune Checkpoint Blockade. *Cell* **167**, 1540 (2016).
59. Rosenberger, F. A. *et al.* Spatial single-cell mass spectrometry defines zonation of the hepatocyte proteome. *Nat Methods* **20**, 1530–1536 (2023).
60. Mardamshina, M. Multiplexed Deep Visual Proteomics Unveils Spatial Heterogeneity and Rare Endocrine States in Human Adult Pancreatic Islets. 1–48 (2025).
61. Stevens, L. E. *et al.* JAK–STAT Signaling in Inflammatory Breast Cancer Enables Chemotherapy-Resistant Cell States. *Cancer Res* **83**, 264–284 (2023).
62. Long, L., Fei, X., Chen, L., Yao, L. & Lei, X. Potential therapeutic targets of the JAK2/STAT3 signaling pathway in triple-negative breast cancer. *Front Oncol* **14**, 1381251 (2024).
63. Zheng, X., Mund, A. & Mann, M. Deciphering functional tumor-immune crosstalk through highly multiplexed imaging and deep visual proteomics. *Mol Cell* **85**, 1008-1023.e7 (2025).
64. Vizcaíno, J. A. *et al.* 2016 update of the PRIDE database and its related tools. *Nucleic Acids Res* **44**, D447–D456 (2016).
65. Tyanova, S. *et al.* The Perseus computational platform for comprehensive analysis of (prote)omics data. *Nature Methods* vol. 13 731–740 Preprint at https://doi.org/10.1038/nmeth.3901 (2016).
66. Sun, L. *et al.* Divenn: An interactive and integrated web-based visualization tool for comparing gene lists. *Front Genet* **10**, (2019).
67. Yu, G., Wang, L. G., Han, Y. & He, Q. Y. ClusterProfiler: An R package for comparing biological themes among gene clusters. *OMICS* **16**, 284–287 (2012).